



UvA-DARE (Digital Academic Repository)

The DBL Survey II

Towards a mass-period distribution of double white dwarf binaries

Munday, James; Pelisoli, Ingrid; Tremblay, Pier-Emmanuel; Jones, David; Nelemans, Gijs; Kilic, Mukremin; Cunningham, Tim; Toonen, Silvia; Santos-García, Alejandro; Dawson, Harry; Pinter, Viktoria; Godson, Benjamin; Martinez, Llanos; Chand, Jaya; Dobson, Ross; Jhass, Kiran; Shenoy, Shravya

DOI

[10.1093/mnras/staf1198](https://doi.org/10.1093/mnras/staf1198)

Publication date

2025

Document Version

Final published version

Published in

Monthly Notices of the Royal Astronomical Society

License

CC BY

[Link to publication](#)

Citation for published version (APA):

Munday, J., Pelisoli, I., Tremblay, P.-E., Jones, D., Nelemans, G., Kilic, M., Cunningham, T., Toonen, S., Santos-García, A., Dawson, H., Pinter, V., Godson, B., Martinez, L., Chand, J., Dobson, R., Jhass, K., & Shenoy, S. (2025). The DBL Survey II: Towards a mass-period distribution of double white dwarf binaries. *Monthly Notices of the Royal Astronomical Society*, 541(4), 3494-3512. <https://doi.org/10.1093/mnras/staf1198>






General rights

It is not permitted to download or to forward/distribute the text or part of it without the consent of the author(s) and/or copyright holder(s), other than for strictly personal, individual use, unless the work is under an open content license (like Creative Commons).

Disclaimer/Complaints regulations

If you believe that digital publication of certain material infringes any of your rights or (privacy) interests, please let the Library know, stating your reasons. In case of a legitimate complaint, the Library will make the material inaccessible and/or remove it from the website. Please Ask the Library: <https://uba.uva.nl/en/contact>, or a letter to: Library of the University of Amsterdam, Secretariat, P.O. Box 19185, 1000 GD Amsterdam, The Netherlands. UvA-DARE is a service provided by the library of the University of Amsterdam (<https://dare.uva.nl>). You will be contacted as soon as possible.

The DBL Survey II: towards a mass–period distribution of double white dwarf binaries

James Munday ¹★, Ingrid Pelisoli ¹, Pier-Emmanuel Tremblay¹, David Jones ^{2,3}, Gijs Nelemans^{4,5,6}, Mukremin Kilic⁷, Tim Cunningham⁸†, Silvia Toonen⁹, Alejandro Santos-García¹⁰, Harry Dawson¹¹, Viktoria Pinter^{12,13}, Benjamin Godson¹, Llanos Martinez¹⁴, Jaya Chand¹⁵, Ross Dobson ¹⁶, Kiran Jhass¹⁷ and Shravya Shenoy ¹⁸

¹Department of Physics, University of Warwick, Gibbet Hill Road, Coventry, CV4 7AL, UK

²Instituto de Astrofísica de Canarias, E-38205 La Laguna, Tenerife, Spain

³Departamento de Astrofísica, Universidad de La Laguna, E-38206 La Laguna, Tenerife, Spain

⁴Department of Astrophysics/IMAPP, Radboud University, PO Box 9010, 6500 GL Nijmegen, The Netherlands

⁵Institute for Astronomy, KU Leuven, Celestijnenlaan 200D, 3001 Leuven, Belgium

⁶SRON, Netherlands Institute for Space Research, Niels Bohrweg 4, 2333 CA Leiden, The Netherlands

⁷Homer L. Dodge Department of Physics and Astronomy, University of Oklahoma, 440 W. Brooks St, Norman, OK 73019, USA

⁸Center for Astrophysics, Harvard & Smithsonian, 60 Garden Street, Cambridge, MA 02138, USA

⁹Anton Pannekoek Institute for Astronomy, University of Amsterdam, 1090 GE Amsterdam, The Netherlands

¹⁰Departament de Física, Universitat Politècnica de Catalunya, c/ Esteve Terrades 5, 08860 Castelldefels, Barcelona, Spain

¹¹Institute for Physics and Astronomy, University of Potsdam, Karl-Liebknecht-Str. 24/25, 14476 Potsdam, Germany

¹²CTAO, Northern Station, Rambla José Ana Fernández Pérez 7, E-38711 Breña Baja, La Palma, Spain

¹³Centro Astronómico Hispano en Andalucía, Observatorio de Calar Alto, Sierra de los Filabres, 04550 Gérgal, Spain

¹⁴Isaac Newton Group of Telescopes, Apartado de Correos 368, E-38700 Santa Cruz de La Palma, Spain

¹⁵Centre for Advanced Instrumentation, Department of Physics, Durham University, South Road, Durham, DH1 3LE, UK

¹⁶Mullard Space Science Laboratory, University College London, Holmbury St Mary, Dorking, Surrey, RH5 6NT, UK

¹⁷Department of Physics and Astronomy, University of Sheffield, Sheffield, S3 7RH, UK

¹⁸Centre for Astrophysics Research, Department of Physics, Astronomy and Mathematics, University of Hertfordshire, Hatfield, Hertfordshire, AL10 9AB, UK

Accepted 2025 July 18. Received 2025 July 17; in original form 2025 June 1

ABSTRACT

Double white dwarf (DWD) binaries are an important remnant of binary evolution as they are possible Type Ia supernova progenitors and strong sources of gravitational waves in the low-frequency regime. The double-lined double white dwarf (DBL) survey searches for compact DWDs where both stars can be spectrally disentangled. Candidates are identified by being overluminous compared to the cooling sequence of a typical-mass, single white dwarf. In this second instalment of the DBL survey, we present full orbital solutions of 15 DWD binaries from our ongoing campaign to accurately measure a magnitude-limited mass–period distribution. For the first time, 12 of these systems are fully solved. A long-standing bias in the full population has been evident, favouring systems with orbital periods up to a few hours, with little exploration of the majority of the compact DWD population, whose orbital period distribution centres at approximately 20 h. The 15 systems in this study span the orbital period range $5 < P_{\text{orb}} < 75$ h, significantly augmenting the number of well-characterized systems over these periods, and in general have two similar mass stars combining to $\approx 1.0 M_{\odot}$. We witness that the orbitally derived mass ratios generally show excellent agreement with those deduced from atmospheric fits to double-lined spectra in previous work, emphasizing the power of wide-scale spectroscopic surveys to efficiently locate the highest-mass, double-lined DWDs in the local Galaxy.

Key words: binaries: spectroscopic – stars: white dwarfs.

1 INTRODUCTION

Double white dwarf (DWD) binaries are one of the end-points of binary star evolution with roughly 100 million DWDs predicted to

exist in the Milky Way alone (Marsh 2011). Two stars can evolve through a near isolated evolution in a wide binary (Heintz et al. 2024), but also there exist many compact DWDs with orbital periods ranging from minutes to days. To be in a compact configuration, such systems have survived at least one common envelope phase (Paczynski 1976; Webbink 1984), making DWDs excellent probes of binary evolution as survivors of prior mass transfer. Furthermore, gravitational wave radiation causes the orbital separation to shrink over long

* E-mail: james.munday98@gmail.com

† NASA Hubble Fellow

time-scales, making DWDs detectable with space-based, millihertz regime gravitational wave detectors (e.g. Lipunov, Postnov & Prokhorov 1987; Nelemans, Yungelson & Portegies Zwart 2001b; Ruiter et al. 2010) such as the Laser Interferometer Space Antenna (LISA; Amaro-Seoane et al. 2017, 2023) or TianQin (Luo et al. 2016). As a result, DWDs can give great insight into general relativistic, or non-general relativistic, orbital decay (Piro 2019; Carvalho et al. 2022; Scherbak & Fuller 2023). Another important characteristic of DWDs is their relevance as one of the long suspected progenitors of Type Ia supernovae (for a recent review, see Ruiter & Seitenzahl 2025); they are enrichers of the galaxy through the production of heavy elements and are used as standard candles. Yet, largely because of the difficulty in observing dim systems, full orbital solutions of very few DWD binaries have been obtained, and the constrained sample is observationally biased with inhomogeneous selection criteria that are difficult to include in model comparisons (e.g. Li et al. 2019).

The current observational sample is far from reflective of the full mass–period distribution of DWD binaries, especially for compact binaries with an orbital period greater than a couple of hours, which is the overwhelming majority of DWDs (e.g. Nelemans et al. 2001a). Worryingly, DWDs with total masses above $1.0 M_{\odot}$ are lacking in the observed sample and, with this, the observed population has fallen short of providing Type Ia progenitors that are near the Chandrasekhar mass limit (Toonen et al. 2017; Rebassa-Mansergas et al. 2019), bringing into doubt whether the double-degenerate pathway is responsible for the majority of Type Ia detonations (see, e.g. Liu, Röpke & Han 2023, and references therein). The extent to which observational biases – particularly those that favour the detection of DWDs with a low-mass component – play a factor in the lack of Type Ia progenitors has long been the main impediment to a fully reflective picture.

The double-lined double white dwarf (DBL) survey was introduced in Munday et al. (2024). A crucial aspect of the survey is to handle observational biases in the compact DWD population by characterizing a magnitude-limited sample with well-defined and understood selection criteria. Without such a deliberate effort, biases are difficult to handle, hampering the accuracy of comparisons to synthetic population models and making it difficult to draw conclusions about the full population of DWDs. As part of this survey, we obtained identification spectra and fitted atmospheric parameters to all observed star systems, resulting in at least 73 per cent of the 117 targets being DWD binaries of any kind. Specifically, the focus of the DBL survey is double-lined DWDs – that is, where a spectral signature from both stars is evident – for which at least a 29 per cent success rate of a source being double-lined was retained. An unveiled class of previously rare massive total mass DWD binaries was recovered, including multiple near- or super-Chandrasekhar total mass DWDs (Munday et al. 2024, 2025). When brought into contact, the fate of the majority of detected systems is to initiate unstable mass transfer, resulting in the merger or pre-merger explosion of sources. The detection of double-lined sources is sensitive to mass ratios of $0.5 \lesssim q \lesssim 2$, with limits due to the fact that the dimmer star must contribute more than approximately 25 per cent of the flux so that it is possible for it to be disentangled spectroscopically.

The objective of this pilot work was the identification of the spectra of a large number of DWD candidates. What remained to be done was phase-resolved spectroscopy of the systems to obtain the orbital periods and hence the underlying period distribution of the double-lined DWD binaries in the sample. Many of the orbital periods are now presented in this study. The follow-up observations that we have undertaken are supplied in Section 2. We give our

fitting methods for extracting radial velocities (RVs) and orbital solutions in Section 3, and in Section 4 we provide the results of our work.

2 OBSERVATIONS

The purpose of our observations was to obtain phase-resolved spectra of the double-lined DA+DA DWDs discovered in Munday et al. (2024), where the Balmer absorption lines of each star can be spectrally disentangled. As the orbital periods were largely unconstrained, and having only the knowledge of a maximum orbital period, our observing strategy was to first obtain two series of three or four consecutive spectra with a gap of a couple of hours between them. Then, a third and fourth series of spectra would be taken in two of the following three nights to improve sensitivity to wider orbits. Together, this meant that we had a starting point of 12–15 spectra per target to resolve the orbital period. For systems where viable aliases were obtained in this time but the exact period alias was unclear, we obtained further observations at a later time with a targeted and dynamic strategy. For example, if strong period aliases appear at 10 and 20 h, we would attempt to obtain spectra of the target with a gap of 5 h. Stronger evidence of the true orbital period would then be ascertained due to the different orbital phase coverages.

Time-series spectra were obtained across 22 nights using the Intermediate Dispersion Spectrograph (IDS) on the 2.5-m Isaac Newton Telescope (INT). We used the R1200R grating centred on $H\alpha$ with a 1.0-arcsec slit, covering the wavelength range of 6000–7130 Å, with a spectral resolution of $R = 6310$ at the centre of $H\alpha$. Observations were carried out over the nights 2019 August 27–September 7, 2019 September 23 and 24, and 2020 June 7–14. An arc frame was taken after the acquisition of each target. For an extended duration on target, arcs were taken every 45 min to correct for flexure. Later, after analysing the majority of these data, we obtained nine nights on the INT from 2024 April 25 to May 3 to resolve the orbits of a few more systems and to improve the solution of certain systems that had multiple viable period aliases. The first four nights utilized the H1800V grating with a 1.4-arcsec slit width (with a DIMM seeing of about 1.0 arcsec), giving a spectral resolution of $R = 9400$, and the other five nights used the same R1200R grating set-up mentioned above. Additional spectra were obtained with the INT across various nights in the years 2023 and 2024 using the R1200B grating, providing a spectral resolution of about $R = 4700$ at $H\beta$. These were reduced with the same method as the R1200R set-up.

Bias frames and tungsten lamp flats were taken at the beginning of each night and used in the data reduction. Spectrophotometric standard stars were also observed at the start or the end of each night to flux calibrate the science exposures and correct for the instrumental response function. When multiple arc frames were taken of a target, the solution to the arcs was interpolated for the mid-exposure time of the science frame for wavelength calibration. All data were reduced using the MOLLY package (Marsh 2019) and spectra were extracted using the method outlined in Marsh (1989). Lastly, we utilized the spectra obtained from the William Herschel Telescope (WHT) of each target, as was presented in Munday et al. (2024).

Once all of these data had been fully and thoroughly analysed, we decided to target the orbital phases of three systems that were close to being solved using the Nordic Optical Telescope (NOT) across the nights 2025 January 23–28 and 2025 May 21–25. The employed instrument set-up was ALFOSC with a g17 grating and a 0.75-arcsec

slit width, giving wavelength coverage of $H\alpha$ at a spectral resolution of $R = 7500$. An arc was taken before each exposure for wavelength calibration, and all data were reduced with the PYPEIT Python package (Prochaska et al. 2020).

Finally, for the target WDJ231404.30+552814.11, nine spectra were taken with the Gemini Multi-Object Spectrograph (GMOS) on Gemini North as part of the queue program GN-2022B-Q-103. Observations were taken over the period 2022 August 3–8 with the R831 grating and a 0.5-arcsec slit to give a spectral resolution of $R = 4396$. Each spectrum had an exposure time of 8 min. A CuAr lamp spectrum was taken after each exposure for wavelength calibration. We used the IRAF GMOS package to reduce these data.

3 METHODS

3.1 Synthetic spectra

To begin with, we used the atmospheric solution of both stars derived in Munday et al. (2024) and maintained the solution fixed to create a synthetic spectrum of both stars. As a base model, we utilized the three-dimensional (3D) non-local thermal equilibrium (NLTE) grid first introduced in Munday et al. (2024), which uses the 3D grids of Tremblay et al. (2013, 2015) together with an NLTE correction that was presented in Kilic, Bédard & Bergeron (2021). The NLTE correction was shown to significantly improve the fit to higher resolution data at $H\alpha$.

The synthetic and observed spectra were normalized to facilitate the processing of ground-based flux-calibrated data. In general, when $T_{\text{eff}} \approx 8000$ K, we chose to normalize Balmer lines using data between wavelengths that correspond to velocities of $\pm(4500\text{--}5000)$ km s⁻¹ for $H\alpha$, $H\beta$, $H\gamma$ and $H\delta$, and $\pm(2000\text{--}2500)$ km s⁻¹ for $H\epsilon$ and $H8$. In WDs cooler than 8000 K, we halved the normalization range to be $\approx \pm(2250\text{--}2500)$ and $\pm(1750\text{--}2000)$ km s⁻¹ for the respective groups of Balmer lines.

3.2 Improved atmospheric constraints on two systems

Since publishing the first DBL survey instalment, we have obtained higher-quality data of two systems presented in Munday et al. (2024). The first is WDJ181058.67+311940.94, which at the time of writing has the largest total mass of any DWD binary ($1.555 \pm 0.044 M_{\odot}$). An investigation devoted to the system was presented in Munday et al. (2025). All data of WDJ181058.67+311940.94 obtained as part of the DBL follow-up were presented in that study, and hence there are no updates to the atmospheric or orbital solution system here. For completeness, the orbital parameters of the system are also presented in this study, as it is a member of the double-lined systems detected in the pilot campaign.

The second system with improved data quality is WDJ170120.99–191527.57. Early analysis of the RVs indicated an orbital period of a few hours, flagging the binary as one of particular interest due to the fast variability of the RVs – hence the extra observation. We used the Magellan Echellette (MagE; Marshall et al. 2008) spectrograph on the 6.5-m Magellan Baade telescope at the Las Campanas Observatory to obtain two consecutive, 1200-s long, high signal-to-noise ratio (S/N) spectra at an orbital phase where the system was at quadrature. The observations were performed using the 0.85-arcsec slit, providing a wavelength coverage of 3700–9300 Å, at a resolving power of $R = 4800$. We obtained three ThAr arc exposures immediately after our science exposures to generate an accurate wavelength solution. The spectroscopic

data were reduced using PYPEIT. We also made use of the MERLIN¹ package, which provides an end-to-end reduction pipeline based on PYPEIT v1.15.0 for MagE spectroscopic data. We hybrid fit these two spectra using an identical method to that presented in Munday et al. (2024) with the 3D-NLTE synthetic spectra grid; the spectral fit is supplied in Figure A1 in the Appendix. This indicates atmospheric parameters of $T_1 = 19780 \pm 270$ K, $\log(g_1) = 8.09 \pm 0.05$ dex, $T_2 = 15490 \pm 260$ K, and $\log(g_2) = 7.87 \pm 0.05$ dex, which should be assumed in any continued analysis of the system. The quoted values include an external error of 1.4 per cent for T_{eff} and 0.042 dex for $\log g$ (Liebert, Bergeron & Holberg 2005) added in quadrature to the formal errors. The new star masses become $M_1 = 0.673 \pm 0.024 M_{\odot}$ and $M_2 = 0.544 \pm 0.022 M_{\odot}$, resulting in a slightly higher total mass ($1.217 \pm 0.032 M_{\odot}$) than previously reported.

3.3 Radial velocities

To determine the RVs, we take the best-fitting atmospheric solution and keep it fixed. Then we convolve the model to the resolution of the observation, and perform a least-squares minimization with the data in the range of ± 20 Å of $H\alpha$. We chose to isolate this wavelength region so that the goodness of fit to the wings of $H\alpha$ does not dominate, as the line core is the primary area of interest to fit RVs. Also, we fit to $H\alpha$ alone because of the much higher resolution in this spectral range for our observations and because the errors induced from imperfect wavelength calibration of data from the blue and red arms of ISIS exceed the benefits of its inclusion.

In a few cases (which are noted and commented on in Section 4), we found that the template spectrum used for RV extraction improves when we instead fit 2-Gaussian profiles to the line cores of each star (that is, two 2-Gaussian profiles, one pair for each star) at the centre of $H\alpha$, on top of a fourth-order polynomial to model the shape of the broad absorption line within 20 Å of its centre. This approach (or similar) has been frequently taken (e.g. Napiwotzki et al. 2002; Nelemans et al. 2005) as a 2-Gaussian model well approximates the shape of the centre of the Balmer absorption features, but the negative is that a fitted polynomial contains no physical information. We decided to employ this method for cases where the shape and depth of the synthetic line core profiles over- or under-fit the observed spectra across all instrumental set-ups. Doing so, we obtained a set of Gaussian parameters that are consistent to all spectra but smeared to the relevant spectral resolution.² A comparison of fits with synthetic spectra and the 2-Gaussian approach is plotted in Fig. 1.

Often, and in our INT data especially, when the site conditions worsened, the continuum S/N is relatively low ($S/N < 20$), leading to an imperfect spectrum normalization. To optimize the normalization, we minimize the residual between the data and the atmospheric fit within 20 Å of the centre of $H\alpha$. Data $\pm 5\text{--}20$ Å away from the centre of $H\alpha$ were sigma-clipped with a threshold of 4σ ; no data within 5 Å of the centre were clipped. RVs and their errors are reported from the median and standard deviation of 1000 bootstrapping iterations. To

¹<https://github.com/vedantchandra/merlin/tree/main>

²The reason for an imperfect atmospheric solution may lie with limitations in the input physics of synthetic grids, an inappropriately chosen mass–temperature–radius relation (carbon–oxygen core versus helium core for WD masses $\approx 0.4\text{--}0.6 M_{\odot}$), which would compromise the apparent-to-absolute-flux scaling factor when fitting photometric data, or a faint tertiary component contributing a small percentage of flux, all of which lead to a too deep/shallow synthetic line core signature

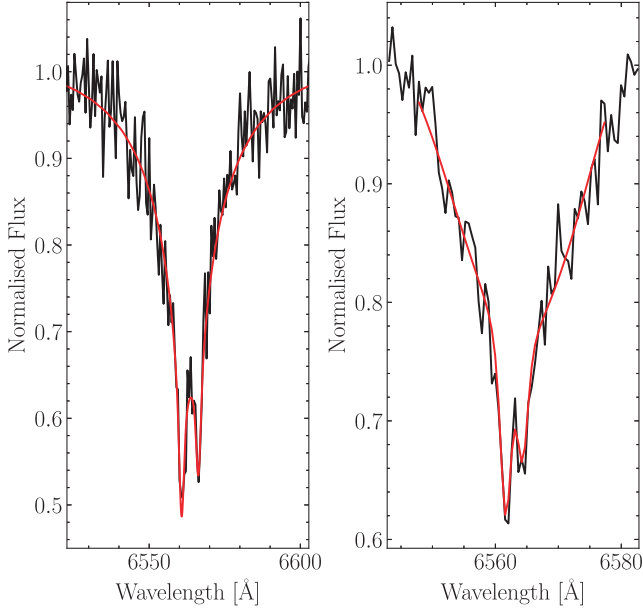


Figure 1. Example fits used to obtain RVs. The spectra are from the INT/IDS, reflecting the quality of the bulk of our data. Left: a best-fitting synthetic spectrum of WDJ005413.14+415613.73 with our formerly presented solution. Both stars have a similar line-core signature and the statistical RV errors for the blueshifted and redshifted stars were 4.5 and 6.1 km s⁻¹, respectively. Right: a case for WDJ163441.85+173634.09 where fitting with two 2-Gaussian components plus an underlying polynomial resulted in a better template to fit to the observations. The statistical RV errors of the blueshifted and redshifted stars were 4.6 and 7.1 km s⁻¹, respectively. Generally, this approach slightly better fits the data but at the expense of losing spectral coverage, which becomes more important to utilize for lower (≈10–15 in continuum) S/N observations. The normalization procedure in the two cases is different, as described in the text.

give an idea of the effect of this optimization, we take the double-lined system WDJ114446.16+364151.13 that has spectra with a wide S/N range and a near-identical spectral signature for both stars at H α . For a noisy spectrum that has S/N = 15 in the continuum and S/N = 8 at the line core centre, the RV errors with no optimizing of the normalization are ± 29.6 and ± 20.1 km s⁻¹; with optimization, the errors are ± 22.6 and 17.7 km s⁻¹ for the two stars. Now, taking the same system but looking at data with S/N = 40 in the continuum and S/N = 25 at the line core centre, no optimizing gives ± 4.8 km s⁻¹ for both stars, while optimizing gives ± 5.0 km s⁻¹ for both stars. In the low S/N data case, the reported RV errors become appreciably better with optimization, whereas the errors are nearly identical when the S/N is higher. Hence, applying this optimized normalization method slightly improved the accuracy and precision of all RVs from low S/N data but made little difference to high S/N data. Furthermore, we note that the scatter in the residual of a sinusoidal fit to the RV curves (which is addressed in Section 3.4) decreased for an optimized normalization, indicating an improved accuracy in the extracted RVs.

3.4 Orbital solutions

A couple of the candidate double-lined systems with time-series spectroscopy are indeed double-lined, but others turned out to be single-lined DWDs. In searching for single-lined RV variability, we invoke the same procedure as in Munday et al. (2024). The mean of all extracted RVs for a source is taken and a null hypothesis, that the RV is a constant with respect to the mean, is tested. We compute the

χ^2 of all measurements compared to the mean and use the relevant χ^2 -distribution for the number of degrees of freedom to calculate the probability that a source is not RV variable, setting a 4σ outlier threshold for variability, equivalent to a false positive probability of 0.62 per cent.

For all RV variable sources, double- or single-lined, we searched for a periodic signal when more than five spectra were taken. This was performed with a least-squares minimization with trial orbital frequencies, f , spaced in a way that no more than 0.01 cycles are skipped over the full baseline of data. The χ^2 of each trial minimization was analysed for a best-fitting solution and the RVs (viewed at time T_{RV}) were modelled following

$$V_{1,2}(\phi) = \gamma_{1,2} \pm K_{1,2} \sin 2\pi\phi, \quad (1)$$

where $\phi = [(T_{RV} - T_0) \bmod f]$ is the orbital phase for each epoch, K is the semi-amplitude, and γ is the RV offset for each star denoted by subscripts 1 and 2. When analysing periodograms, we normalize the χ^2 of the best trial solution for each frequency to obtain a power spectrum following (Cumming 2004):

$$z_{Kep}(f) = \frac{N - 5}{4} \frac{\chi_0^2 - \chi^2(f)}{\chi^2(f)} \quad (2)$$

where N is the number of epochs and χ_0^2 is χ^2 with respect to the weighted mean of the RV measurements (whereas χ^2 is with the best Keplerian orbital fit). For double-lined fits, the RVs and weighted means from the two stars are handled separately and summed after. When the power z_{Kep} is maximized, the χ^2 is minimized.

A strength of having the unique spectral signature and atmospheric parameters of both stars in double-lined sources is that we can furthermore use physical insight of the system to limit the maximum constraint of $K_{1,2}$ for each trial frequency. A minimum and maximum K_{max} can be inferred from the binary mass function with the expectation that the stars are circularized, using

$$PK_{max}^3 = \frac{2\pi G M_{max}^3 \sin(i = 90^\circ)^3}{(M_{min} + M_{max})^2}. \quad (3)$$

Here, for a DWD system, a sub-Chandrasekhar mass limit $M_{max} = 1.4 M_\odot$ and a minimum WD mass of $M_{min} \approx 0.15 M_\odot$ (Istrate et al. 2016; Calcaferro, Althaus & Córscico 2018) are applied, to put upper and lower limits on $K_{1,2}$, respectively. For single-lined WD binaries, the companion may be a neutron star with maximum mass of approximately $3.0 M_\odot$ (e.g. Kalogera & Baym 1996), and hence $M_{min} = 0.15 M_\odot$ and $M_{max} = 3.0 M_\odot$ apply. Black hole companions to a WD are not expected in the sample because of their much smaller predicted number in the Galaxy (Nelemans et al. 2001b) and they would only be applicable to systems that spectrally appear as a single WD (no excess flux). Additional restrictions can be applied to place limits on the orbital inclination, i , if photometric variability is or is not witnessed (Section 3.5), causing PK_{max}^3 to alter. Similarly, in this case, a constraint on PK_{min}^3 could be applied.

We also limited the range of valid orbital solutions based on the details of the spectral fit, again possible from the double-lined nature of these sources. The difference between γ_1 and γ_2 is equal to the difference in gravitational redshifts and, as such,

$$\gamma_2 - \gamma_1 = \frac{G}{c} \left(\frac{M_2}{R_2} - \frac{M_1}{R_1} \right) = \frac{G}{c} \left(\frac{K_1 M_1 / K_2}{R_2} - \frac{M_1}{R_1} \right) \quad (4)$$

with star radii (R) predictable from mass–radius relationships. With this and the atmospheric solutions for each system, we decided to take the conservative approach of applying a flat prior on the relative gravitational redshift spanning 3σ from the median solution

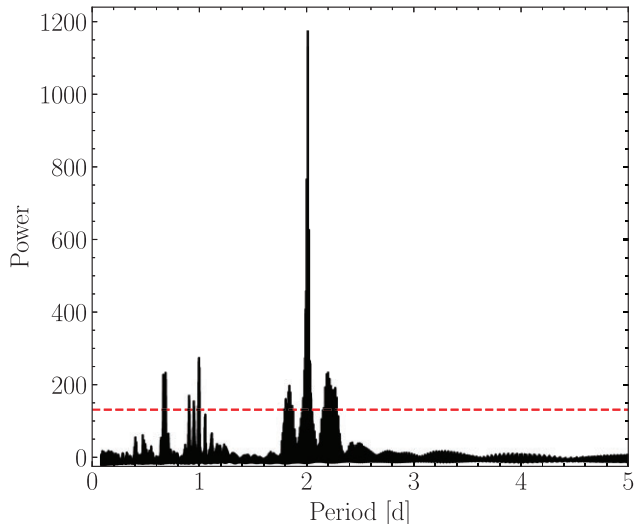


Figure 2. An example Lomb–Scargle periodogram showing that of WDJ020847.22+251409.97. The spacing between trial frequencies is chosen such that no more than 0.01 cycles are skipped across the full time baseline between adjacent solutions. The dashed red horizontal line shows the false alarm probability at a 4σ level. Multiple peaks lie above the 4σ level and are a consequence of the wide spacing of observation and certain aliases that better fit the RVs of just one of the stars. However, the non-highest peaks clearly show blocks of observations that lie off the sinusoidal trend upon visual inspection. This isolates the true orbital period of 2.008 d (48.1837 h).

for both the masses and the radii of each star. The typical mass errors are $\pm 0.04 M_{\odot}$ and, while we previously assumed a thick hydrogen envelope consistent with single-star evolutionary tracks to scale to an Eddington flux, the size of the hydrogen envelopes is largely unknown. With that in mind, 3σ errors on the interpolated radii were again appropriate to incorporate the uncertainty in the model fit. We note that this is an intentionally cautious approach and was chosen in case an incorrect atmospheric solution is found from a local minimum. The restriction on the difference of gravitational redshifts served to remove spurious periodogram solutions when finding a best-fitting solution.

We calculated false alarm probabilities for each system to analyse the significance of each peak in the power spectrum. This was performed through a bootstrap approach by randomly shuffling the timestamps of observation, recalculating Lomb–Scargle periodograms (Lomb 1976; Scargle 1982) over 50 iterations and taking quantiles of the full array of powers from these 50 iterations as the false alarm probability. We consider a trial period to be the true period of the system if there is a unique peak above a 4σ false alarm probability and 3σ for a peak to be considered an alias or the true period. Below those thresholds, the period is not completely solved but we assign limits on the maximum/minimum orbital period based on the information currently extractable by taking the upper/lower boundaries where no period aliases fall above a 2σ false alarm probability. Here, further RV measurements would be required to fully solve the orbits. In cases where there is more than one peak above the 4σ or 3σ alarm probability, we inspect all individual peaks to look for a cause and to assess if any of these solutions are suitable. When this happened, it often was an artefact of the wide time spacing between observations, but all cases where this occurred are commented on in Section 4. An example periodogram for a solved system is shown in Fig. 2.

3.5 Light curves

We analysed time-series archival photometry from the *Transiting Exoplanet Survey Satellite* (TESS; Ricker et al. 2015), Zwicky Transient Facility (ZTF; Bellm et al. 2019), the Catalina Real-time Transient Survey (Drake et al. 2009), *Gaia* (Gaia Collaboration et al. 2023), and the Asteroid Terrestrial-impact Last Alert System (Tonry et al. 2018) to search for photometric variability amongst the full selection of DWDs.³ The brightest of our sources saturate in some of these surveys and, when they are saturating, time-series photometry was ignored. Sources in *Gaia* listed as variable have available photometric data for download as of data release 3 and, in these cases, the *Gaia* photometry was analysed. *TESS* light curves in the fast, short and long cadences were obtained when available from the MAST system, and we extracted the photometry from *TESS* pixel frames when not available (typically for sources dimmer than 16 mag).

Finally, we note that *TESS* (all cadences) and ZTF (in filters g , r , i) photometry was inspected for all systems with solved periods by searching for variability within 2 per cent of the orbital period. The same was performed for all aliases of systems that have more than one above the false alarm probability, described in Section 4.2. In no case was a significant photometric signal observed for a one-term Lomb–Scargle or a box least-squares periodogram. The use of a one-term Lomb–Scargle periodogram is most appropriate for identifying Doppler beaming, tidal deformation or irradiation, which will be the strongest orbitally induced variability in all systems (Hermes et al. 2014), whereas a box least-squares periodogram could reveal the unlikely event of eclipses, requiring an almost perfectly edge-on inclination for the typical DWD binary. Gravitational lensing is unlikely to occur or be detected (Marsh 2001; Sajadian 2025).

4 RESULTS

We present here an overview of all systems that now have full atmospheric (Munday et al. 2024) and orbital solutions. In this section, we discuss newly presented results as well as results obtained in prior work.⁴ We particularly emphasize here that the full population of compact DWDs are expected to have a median period of about 20 h, as found through synthetic binary population synthesis models (Nelemans et al. 2001a).

It should be noted that inter-night observations cause a decreased efficiency in solving orbital periods because of the consequent window function. For example, periods of 8, 12, 24, and 48 h, etc., are more challenging to solve. Multiple-day orbital periods are also more challenging to ascertain because our strategy of taking three consecutive spectra does not cover as large a range of orbital phase. The selection of systems from the 34 double-lined systems we found in Munday et al. (2024) is largely random, with the only restriction being the visibility for the scheduled telescope nights and the need for both stars to be separable at a spectral resolution of $R = 6310$. Lastly, there is sensitivity to the full range of orbital periods above

³<https://github.com/JamesMunday98/AllSurveyPhotometry>

⁴In Munday et al. (2025), we noted that the RVs of spectra with spectral resolution $R < 10000$ were slightly inaccurate ($5\text{--}10 \text{ km s}^{-1}$) when spectral lines perfectly overlap at the time of observation, and so were removed when solving for the orbital solution. Here however, we choose not to disregard any RVs that fall into this category because, with approximately 15–20 RVs per system, the information gained by including them in settling period aliases is far beneficial. One should consider their removal if more RVs are obtained in future work.

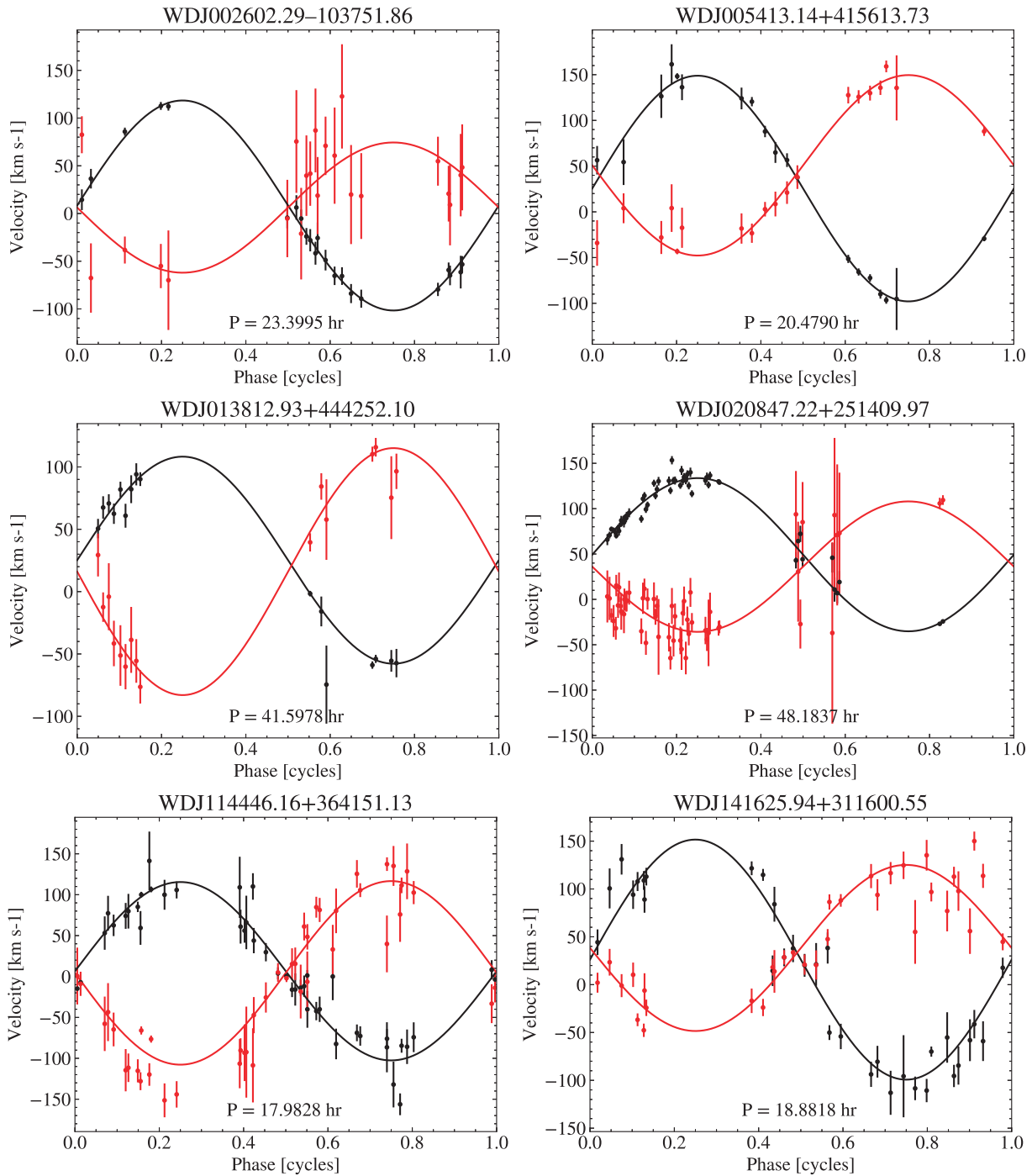


Figure 3. RV curves of all double-lined systems with orbital solutions presented in this study. The data points and the curves in black represent the hotter star and those in red are for the cooler star. The details of each solution are given and described in text. Titles above each plot show the system that each curve corresponds to, while the orbital period is mentioned at the bottom of each plot for convenience. The velocity for each point here has been corrected for relativistic effects and therefore is not an observed velocity (Appendix B).

2 h (with this minimum set because of orbital smearing across 30 min exposure times) and orbital periods are sampled up to 10 d.

4.1 Solved periods

The list of fully solved systems are as follows, with comments on the validity of the results when comparing the atmospheric and orbital

solutions. The RV curves for each are plotted in Figs 3 and 4, with the exact orbital parameters given in Table 1. Merger times are mentioned when the orbital period is below 15 h using Peters’ equation (Peters 1964) for a circular orbit. The double-lined systems here are 15 of the 34 presented in Munday et al. (2024), while the first discovery of three of them was in other studies. RVs for each source are presented in Appendix B.

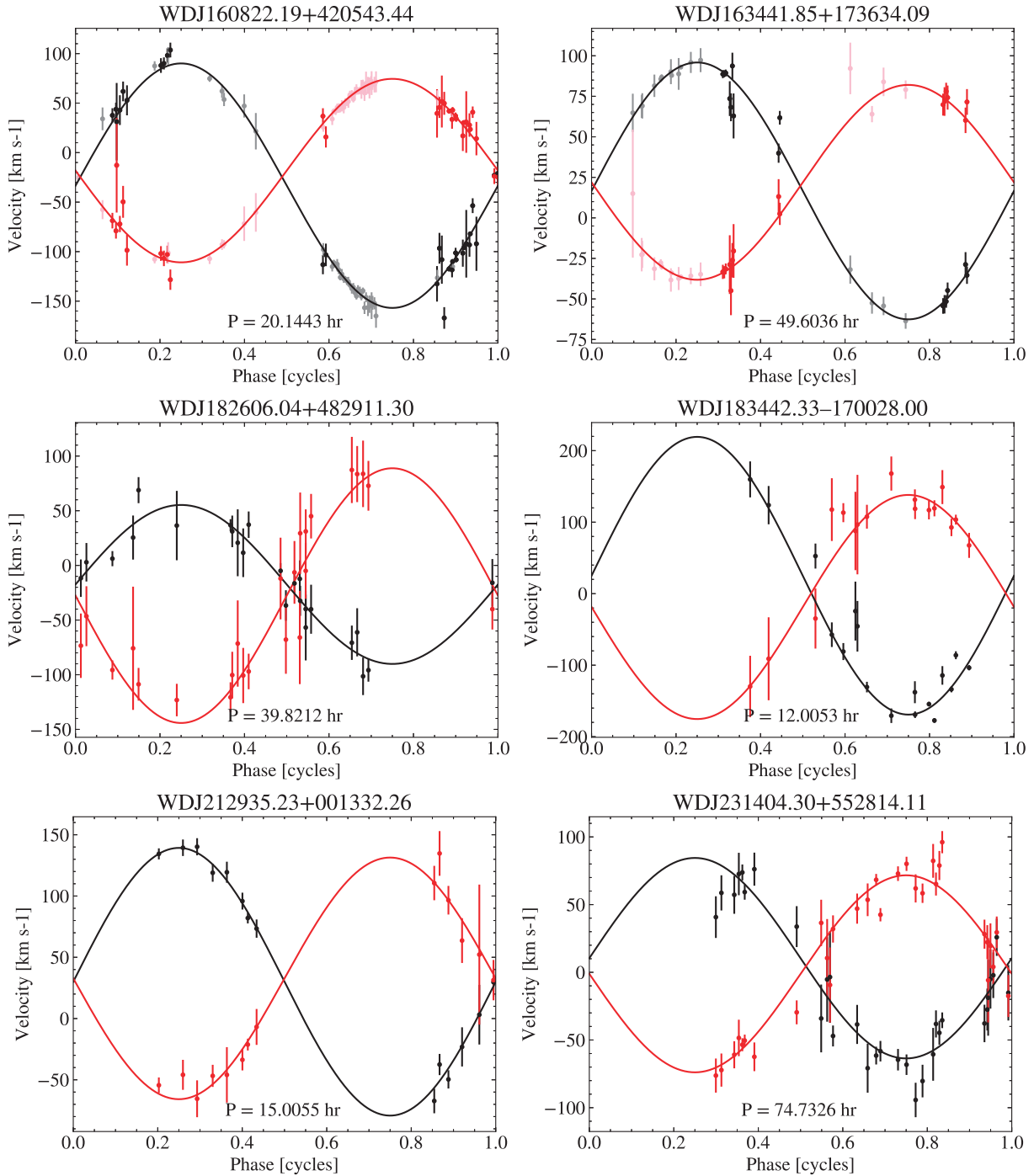


Figure 4. RV curves of the other six systems presented in this work, continuing from Fig. 3. The data for the hotter and cooler star of the binary are plotted in black and red, respectively. WDJ153615.83+501350.98 is omitted from the plots as we only had two further RV measurements to add to those in Kilic et al. (2021), whereas for WDJ160822.19+420543.44 and WDJ163441.85+173634.09 we were able to recover the same orbital solutions in this work with a much larger number of RVs to add. The RVs presented in Kilic et al. (2020, 2021) for these two systems were incorporated into our analysis, plotted in light red/black shades. The system WDJ151109.90+404801.18 is also omitted given its unclear orbital solution, even though the correct period alias has been identified.

WDJ002602.29–103751.86 has one peak above 4σ and one other close to this threshold, lying at 23.40 and 7.91 h, respectively. The first of these clearly best fits the RVs of the brighter star and has a near-zero difference in gravitational redshift, while the other solution slightly better fits RVs for the dimmer star and has a gravitational redshift difference of 10–20 km s⁻¹. We strongly

expect that the true period is 23.40 h because of the better fit and accordance with the atmospheric solution, and hence we adopt this value. This leads to the system having an orbitally derived mass ratio of $q = K_2/K_1 = 0.62 \pm 0.27$, while the atmospheric mass ratio is $q = M_1/M_2 = 1.12 \pm 0.07$, which is significantly different. This difference cannot be resolved by forcing a carbon–oxygen or helium-

core mass–radius relationship in the atmospheric fit, as this still leads to a poor match to the observations for all combinations. The detection of the dimmer star is marginal at H α and the fractional flux contributed in other wavelengths is small; further RVs, and perhaps higher S/N observations at quadrature with H α , are encouraged to improve the accuracy of K_2 . The Gaussians plus polynomial template proved advantageous in obtaining more precise RVs due to the slight detection of the cooler WD in this system.

WDJ005413.14+415613.73 has an orbital period of 20.48 h, with an orbitally derived mass ratio $q = K_2/K_1 = 0.78 \pm 0.08$ and the atmospheric solution represents $q = 0.96 \pm 0.12$.

WDJ013812.93+444252.10 has an orbital period of 41.60 h, with an orbitally derived mass ratio $q = K_2/K_1 = 1.19 \pm 0.27$ and the atmospheric solution represents $q = 1.08 \pm 0.07$.

WDJ020847.22+251409.97 is the closest new double-lined DWD in the DBL survey, located at 39 pc, formerly identified as a double degenerate candidate in the 40 pc survey of WDs (McCleery et al. 2020). We find that it has an orbital period of 48.18 h, the atmospheric solution represents $q = M_1/M_2 = 0.74 \pm 0.04$ and the orbital solution $q = K_2/K_1 = 0.85 \pm 0.11$. The Gaussians plus polynomial method was used to extract RVs, again because of the slight detection of the cooler WD.

WDJ114446.16+364151.13 has an orbital period of 17.98 h, with an orbitally derived mass ratio $q = K_1/K_2 = 1.03 \pm 0.15$ and the atmospheric solution represents $q = 0.93 \pm 0.09$.

WDJ141625.94+311600.55 has an orbital period of 18.88 h, with an orbitally derived mass ratio $q = K_2/K_1 = 0.69 \pm 0.12$ and the mass ratio from the atmospheric solution is $q = 1.23 \pm 0.10$. The two stars are near identical in terms of their atmospheric parameters and their spectral signature. If we switch the RV assignments such that the hotter star is given the RVs of the star that was previously thought to be cooler, we obtain atmospheric parameters of $T_{1,\text{eff}} = 13\,460 \pm 400$ K, $T_{2,\text{eff}} = 12\,740 \pm 250$ K, $\log(g_1) = 7.66 \pm 0.16$ dex, $\log(g_2) = 7.70 \pm 0.15$ dex, $M_1 = 0.44 \pm 0.05 M_\odot$, and $M_2 = 0.45 \pm 0.05 M_\odot$. This generates an atmospheric mass ratio of $q = 0.98 \pm 0.16$, which far better aligns with the orbital solution, so we assume these new atmospheric parameters going forward.

WDJ151109.90+404801.18 is an interesting case where, for five of the 23 spectra (three on one night, two on another), we are not able to determine which star is which in the double-lined spectra, even when trialling every valid combination of RV assignments. The reason for this is that the spectral signature from both stars at H α is very similar. However, what is common to all trial combinations is that an orbital period of approximately 23.3–23.6 h is clearly the highest and the only peak that is high in power, making an orbital period in this range the correct solution for this binary. The short-term RV variability of a group of six spectra on the same night covering a 4.8-h observing window affirms that the near 1-d orbital period is a true detection. At times, and depending on the assignment of the unclear RVs, another peak at half of this period emerges, but this fits well the RVs of only one of the stars. For the 23.3–23.6 h period aliases, we find that $q = K_2/K_1 \approx 1.0$ –1.5 in all cases, but the error on q is approximately ± 0.4 –0.5 and so it is largely unconstrained. The high percentage error stems from the poor phase coverage given the near 1-d orbital period; however, because of the similar spectral signature from both stars, conclusively resolving the orbital parameters of this binary would be very challenging unless devoting entire telescope nights to its observation. In Appendix B, we note the RVs that are unclear. The atmospheric solution for this system gives $q = 1.52 \pm 0.11$, which is in the general vicinity of the orbital solution. The Gaussians plus polynomial method

was used to measure RVs because the template fit to the line core shapes was improved for these stars with a similar line core signature.

WDJ153615.83+501350.98, or **WD 1534+503**, was discovered and published before completion of this work (Kilic et al. 2021). We only have two additional RV measurements from the identification spectra for this system, which we obtained using the Gaussians plus polynomial method. Combining data sets, we find $P_{\text{orb}} = 17.02$ h. This orbital period has a greatly improved precision in comparison to previously published work, given the extra year in the time baseline of the new RV measurements. We next quote our orbital solution, though we emphasize that differences in the fitting procedure between their work and ours, and the instrumental set-ups/data reduction, could lead to systematic errors in the results. We find $K_1 = 135.08 \pm 4.27$ km s $^{-1}$, $K_2 = 89.15 \pm 9.88$ km s $^{-1}$, $\gamma_1 = 23.22 \pm 3.22$ km s $^{-1}$, and $\gamma_2 = 44.45 \pm 7.00$ km s $^{-1}$. The orbital solution hence indicates $q = K_2/K_1 = 0.660 \pm 0.076$. This remains in good agreement with the atmospheric solution presented in Kilic et al. (2021), which was $q = M_1/M_2 = 0.64 \pm 0.15$, but less so with that of Munday et al. (2024), which was $q = M_1/M_2 = 0.96 \pm 0.07$. The difference likely stems from the choice of mass–radius relationships employed, in such a way that the lower-mass star’s radius does not align well with a helium-core WD model. It may be a carbon–oxygen or a hybrid core, and the orbital solution hence encourages adoption of the atmospheric solution in Kilic et al. (2021).

WDJ160822.19+420543.44, or **WD 1606+422**, was independently discovered and published before completion of this work (Kilic et al. 2020). To verify the orbital solution found by these authors with a unique data set, we used our 30 RV measurements of the binary and found a solution consistent with their results. Maintaining the same convention that star 1 is the hotter star and given the excellent agreement, we decided to merge the data sets to improve the orbital solution further. Overall, we arrive at a solution of a 20.14-h orbital period with $K_1 = 92.60 \pm 2.45$ km s $^{-1}$, $K_2 = 127.24 \pm 2.30$ km s $^{-1}$, $\gamma_1 = -18.04 \pm 1.65$ km s $^{-1}$, and $\gamma_2 = -31.40 \pm 1.57$ km s $^{-1}$. With this, the newfound mass ratio from the orbital solution is $q = K_2/K_1 = 1.37 \pm 0.04$. Our atmospheric solution suggests $q = M_1/M_2 = 1.17 \pm 0.08$, and with this all results are consistent.

WDJ163441.85+173634.09, or **PG 1632+177**, was also independently discovered and published by Kilic et al. (2021) and again we find consistency between our atmospheric solution and theirs. Given a non-ideal atmospheric fit to the H α line cores for this binary, we decided to fit the RVs with the Gaussians plus polynomial method. The orbital solution from the RVs from both studies with our additional 14 RV measurements gives an orbital period of 49.60 h, $K_1 = 79.63 \pm 1.73$ km s $^{-1}$, $K_2 = -60.59 \pm 1.74$ km s $^{-1}$, $\gamma_1 = 16.21 \pm 1.79$ km s $^{-1}$, and $\gamma_2 = 22.38 \pm 1.44$ km s $^{-1}$. This system is another case where the mass of one of the stars is on the boundary between a CO or He-core WD, resulting in a large discrepancy between M_1/M_2 and K_2/K_1 . The solution presented in Kilic et al. (2021) better fits the data for which the lower-mass WD with $M_1 = 0.392_{-0.059}^{+0.069} M_\odot$ has a hybrid He/CO or a CO core and the larger-mass WD has a mass $M_2 = 0.526_{-0.082}^{+0.095} M_\odot$. We continue to encourage the use of this result, making the atmospheric $q = M_1/M_2 = 0.75 \pm 0.18$ and the newly found orbital with an improved precision on the orbital period $q = K_2/K_1 = 0.761 \pm 0.027$.

WDJ181058.67+311940.94, as presented in Munday et al. (2025), has an orbital period of 14.24 h, with an orbitally derived mass ratio $q = K_2/K_1 = 0.98 \pm 0.03$ and the updated atmospheric solution represents $q = 0.86 \pm 0.04$. Its merger time is 22.6 ± 1.0 Gyr.

WDJ182606.04+482911.30 has an orbital period of 39.82 h, with an orbitally derived mass ratio $q = K_2/K_1 = 1.60 \pm 0.29$ and an atmospheric solution giving $q = 0.87 \pm 0.12$. In this case, we found three periodogram peaks above the 4σ false alarm probability threshold, but inspection of the RV curve for the two lower aliases shows a largely spurious result with only the RVs of the brighter star being well fit, and so they can be rejected. This leaves only the 39.82-h peak as a valid solution. The spectral fit for the atmospheric solution appears very good, though with a slightly over-predicted synthetic photometry in the blue. *Gaia* photometry alone was used as there are two entries of the same source in PanSTARRS with reported magnitudes that slightly conflict, but when fitting just the spectra we obtain a very similar best-fitting atmospheric solution. The reason for this large discrepancy in mass ratios eludes us, and we hope that future photometric/astrometric survey data releases or an improved precision on the orbital solution will aid in finding consistency in the future.

WDJ183442.33–170028.00 had three solutions above the 4σ false alarm probability. All fit the RVs from the hotter star well, but only the highest power peak also fits the RVs from the cooler WD, leaving one unique and valid solution. The source has an orbital period of 12.01 h, with an orbitally derived mass ratio $q = K_2/K_1 = 0.807 \pm 0.468$ and the atmospheric solution represents $q = M_1/M_2 = 0.91 \pm 0.07$. The system is a unique case amongst the current DBL survey sample, having strong emission at $H\alpha$ that is not RV variable and likely originates from an unrelated hydrogen cloud, given the location of the field. This severely jeopardizes the precision of RVs from the secondary, leading to the high uncertainty on the orbital mass ratio. However, the found orbital solution is consistent with the atmospheric solution, and so we continue with the assumption that the atmospherically deduced masses of both WDs are accurate. At approximately $0.4 M_\odot$ each, both stars are relatively low mass compared with the rest of the double-lined sample, and the merger time is 43 ± 4 Gyr.

WDJ212935.23+001332.26 has an orbital period of 15.01 h, with an orbitally derived mass ratio $q = K_1/K_2 = 0.90 \pm 0.11$ and an atmospheric solution giving $q = 1.00 \pm 0.10$. The Gaussians plus polynomial method was better and was used here to extract RVs because of an inadequate atmospheric fit to the $H\alpha$ line cores.

WDJ231404.30+552814.11 has an orbital period of 74.73 h, making it the largest orbital period of all system solutions presented in this work. The orbital mass ratio is $q = K_2/K_1 = 0.99 \pm 0.13$ while the atmospheric solution gives $q = 1.74 \pm 0.12$, which is a striking discrepancy. With this, we decided to refit the atmospheric solution with a forced carbon–oxygen core relation for both stars, although no combination of synthetic spectra agrees with the orbital solution, while performing hybrid fitting to the photometry, parallax and spectroscopy of the source. If we fit to the spectroscopy only and with a forced carbon–oxygen mass–radius relationship, the fit appreciably improves in all Balmer lines besides $H\alpha$ and we are able to find an improved agreement with the orbital solution. The parameters we find are $T_1 = 13770 \pm 210$ K, $T_2 = 8260 \pm 190$ K, $\log(g_1) = 7.86 \pm 0.05$ dex, and $\log(g_2) = 7.64 \pm 0.04$ dex, making $M_1 = 0.53 \pm 0.03 M_\odot$ and $M_2 = 0.44 \pm 0.01 M_\odot$. The distance (taken as the inverse of the parallax) is 105.0 ± 0.3 pc for our fitted solution and 105.5 ± 0.4 pc using the *Gaia* DR3 parallax. The mass ratio of the new atmospheric solution becomes $q = M_1/M_2 = 1.20 \pm 0.07$ and we find consistency between the atmospheric and orbital solutions. With that in mind, we encourage the use of this atmospheric solution, which ignores the photometry and parallax of the source. In measuring RVs, we used the Gaussians plus polynomial model as it resulted in an improved accuracy and is independent of the best-fitting synthetic spectra.

4.2 Systems with period aliases and constraints

Similar to before, here we address the systems where our RVs restrict the valid orbital solution of the binary by describing potential aliases. We present a further five of the 34 double-lined systems that we identified, plus details of a sixth source, which was formerly considered a candidate double-lined system and is now verified as double-lined. RVs for each source are presented in Appendix C.

WDJ000319.54+022623.28 has 17 RV measurements of each star recorded and has two peaks above the 4σ false alarm probability, where it is difficult to separate which is correct. The peak of highest power is at a 14.55-h orbital period and the other at a 37.06-h orbital period. The relative flux difference between the $H\alpha$ line cores is large, meaning that, with approximately three to five more RV measurements closely separated in time, the true solution would be easily solvable in future work. Relatively uneven RV phase coverage leads to a large orbitally derived mass ratio of about $q = K_2/K_1 \approx 1.9$ in both cases, but we promote more observations before drawing any further conclusions.

WDJ080856.79+461300.08 has one unique peak above the 4σ false alarm probability that poorly covers the orbital phase space, with an orbital period of 21.93 h. However, there is another peak with relatively high power at 19.48 h, which appears suitable, leading us to categorize this as a system with aliases. Further smaller and similar height peaks exist in the periodogram in the range of 60–110 h, but they do not account for the short-term RV variability that is clearly noticed, with the peaks likely appearing because of the window function of our widely spaced observations. An orbital period of about 20 h seems the most likely solution, where the 21.93-h alias has $q = K_2/K_1 = 1.17 \pm 0.20$ and the 19.48-h alias has $q = 1.15 \pm 0.33$, both consistent with that indicated from the atmospheric solution, which is $q = 1.28 \pm 0.08$. The Gaussians plus polynomial method was used in obtaining RVs as the line core fit was significantly better.

WDJ170120.99–191527.57 reveals the most compact orbital period of all systems presented in this work, but its true orbital period is not clear. Good orbital solutions are obtained above the 4σ alarm probability for 4.95-, 6.24-, and 4.10-h orbital periods, in order of periodogram peak power. A few out-of-phase points are witnessed in the RV curve for an 8.43-h period, which has about a third of the power as the other three peaks, but it is still significant. All of these solutions have an orbital mass ratio of $q \approx 0.85$ – 0.9 , while the atmospheric masses were found to be 0.673 ± 0.024 and $0.544 \pm 0.022 M_\odot$ (Section 3.2), and with this the atmospheric solution is $q = M_1/M_2 = 1.24 \pm 0.07$. For all of these orbital period aliases, the merger time of the system must be within a few Gyr.

WDJ180115.37+721848.76 has 10 RV measurements in total, which are relatively few to solve an orbit, and with this the periodogram is inconclusive. The true alias of the DWD would be easy to resolve with just a couple more measurements even with a long time spacing, given the clear shape of the $H\alpha$ line cores at a spectral resolution of $R = 6310$. The atmospheric solution gives $q = 0.89 \pm 0.05$, which aligns with the semi-amplitude ratio for the highest-power aliases, but for now we can only conclude that the orbital period is very likely between 6 and 40 h.

WDJ221209.01+612906.96 has nine RVs for each star. The spectral signature of each star is very similar, making it challenging to correctly assign to the hotter or cooler star at each epoch too. We tried all combinations of assignments possible, but without clear periodogram aliases appearing in all cases. Little can be said except that the orbital period is more than 3 h and the maximum possible period based on the binary mass function and the maximum perceived

Table 1. Measured orbital parameters for each system. For WDJ151109.90+404801.18, the period alias is resolved but some RV measurements are unclear, leading us not to present detailed orbital parameters or T_0 .

Name	Period (d)	$T_0 - 245\,0000$ (HJD, UTC)	K_1 (km s $^{-1}$)	K_2 (km s $^{-1}$)	γ_1 (km s $^{-1}$)	γ_2 (km s $^{-1}$)
WDJ002602.29−103751.86	0.9749777(58)	8358.5743(60)	110.1 ± 5.8	68.3 ± 29.4	8.4 ± 3.4	6.2 ± 15.7
WDJ005413.14+415613.73	0.853294(70)	8358.232(58)	127.4 ± 5.0	99.0 ± 8.9	26.3 ± 3.1	51.0 ± 6.1
WDJ013812.93+444252.10	1.73324(13)	8357.016(21)	81.9 ± 9.7	97.5 ± 18.9	25.1 ± 3.6	17.4 ± 9.8
WDJ020847.22+251409.97	2.007653(28)	8357.064(13)	84.4 ± 3.3	71.9 ± 9.0	49.1 ± 3.3	36.2 ± 6.9
WDJ114446.16+364151.13	0.7492851(65)	8645.273(12)	108.6 ± 10.8	111.7 ± 12.4	6.5 ± 6.0	4.5 ± 9.2
WDJ141625.94+311600.55	0.7867420(15)	8589.519(25)	125.5 ± 12.4	86.9 ± 13.1	26.0 ± 9.2	38.3 ± 8.4
WDJ151109.90+404801.18	≈ 0.97–0.99	–	–	–	–	–
WDJ153615.83+501350.98	0.709254(48)	8287.808(29)	135.1 ± 4.3	89.2 ± 9.9	23.2 ± 3.2	44.5 ± 7.0
WDJ160822.19+420543.44	0.8393438(36)	8281.5690(18)	92.6 ± 2.5	127.24 ± 2.30	−18.0 ± 1.7	−31.4 ± 1.6
WDJ163441.85+173634.09	2.066817(44)	8281.2062(80)	79.6 ± 1.7	60.6 ± 1.7	16.2 ± 1.8	22.4 ± 1.4
WDJ181058.67+311940.94	0.5931479(9)	8587.6663(18)	93.9 ± 2.0	95.7 ± 2.1	50.0 ± 1.5	53.5 ± 1.6
WDJ182606.04+482911.30	1.659219(28)	8358.620(25)	72.7 ± 9.3	116.6 ± 14.9	−17.3 ± 6.4	−27.5 ± 10.2
WDJ183442.33−170028.00	0.5002200(39)	8359.9874(54)	194.2 ± 29.1	156.7 ± 87.8	25.1 ± 25.2	−18.6 ± 73.2
WDJ212935.23+001332.26	0.6252288(96)	8359.3171(76)	108.2 ± 6.9	97.5 ± 10.0	31.4 ± 4.6	32.6 ± 6.9
WDJ231404.30+552814.11	3.11386(15)	8358.422(48)	74.1 ± 7.8	73.2 ± 6.1	10.9 ± 6.4	−1.7 ± 5.7

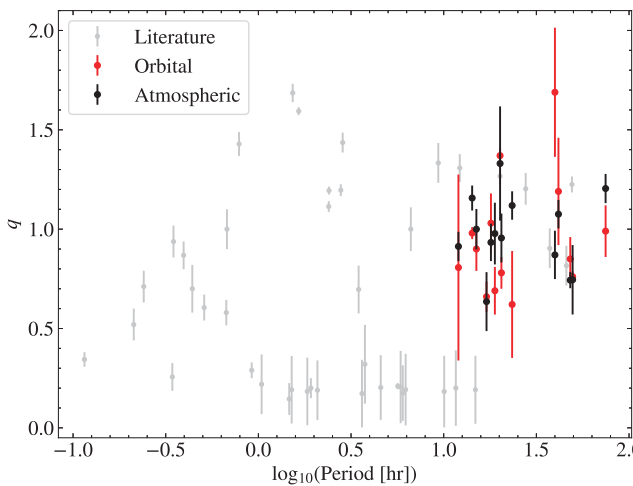


Figure 5. A comparison of the orbital and atmospheric mass ratios against the orbital period. The mass ratios of other previously studied DWDs are included in grey to show the overall observed mass ratio versus period distribution of DWDs. Mass ratios of the double-lined DWDs found in the DBL survey are limited to approximately $q = 0.5$ – 2.0 .

RV split between the stars is 13.5 d. With the lack of certainty around the correct star at each epoch, we choose not to present the measured RVs for these systems.

WDJ234929.57+102255.57 was originally categorized as a candidate double-lined DWD in Munday et al. (2024). Further spectra clearly indicate a double-lined DWD, affirming the presumption. The periodogram of our seven RV measurements give strong evidence in favour of an orbital period above 24 h, with prominent aliases of 27.49, 53.81, and 61.01 h. The latter two solutions have an orbital mass $q \approx 1$, which would align well with the atmospheric solution, but the small number of spectra at hand are insufficient to draw a robust conclusion.

4.3 Follow-up of candidate double-lined DWDs and single-lined systems

Further observations of a couple of single-lined targets were taken to probe RV variability when no other good targets were ob-

servable given the time and conditions of the night, but all of them resulted in no firm detection of binarity. These consist of three spectra of WDJ185640.86+120844.61 and ten spectra of WDJ192817.81+354442.60. The extra RV measurements for these systems, as well as all RVs for the single-lined systems presented in Munday et al. (2024), are presented in Appendix D.

5 DISCUSSION

With many new orbital solutions presented, we turn our attention towards making comparisons with the full sample of published DWD binaries.⁵ We emphasize again that the choice of which double-lined systems were followed up for time-series RVs was purely based upon which were observable for the allocated telescope nights and for systems where both stars would be separable at the slightly lower spectral resolution of the INT observations. Hence, the sampling of systems from the full list of double-lined DWDs in the DBL survey is relatively random, including the outlier in total mass WDJ181058.67+311940.94, which was the highest total mass system discovered.

Fig. 5 shows the orbital period and mass ratio distribution of the observed sample. As is clear from the previous section and Fig. 5, these DWD binaries group around an orbital mass ratio of $q = 1$. This is an unsurprising observational bias of the survey, given that two similar stars are easiest to detect as a double-lined source DWD. The newly discovered systems populate a period space that was previously sparsely sampled. Their range of periods aligns well with predictions from recent synthetic populations, which forecast an abundance of $q \approx 1$ DWDs at certain periods (Ge et al. 2010, 2015, 2020; Toonen, Nelemans & Portegies Zwart 2012; Li et al. 2023). In the vast majority of cases, we see that the orbital and atmospheric mass ratios agree well (Figs 5 and 6), emphasizing the general accuracy of the masses of double-lined DWDs obtained from identification spectra alone when fitting full-visible spectroscopy in combination with absolute photometry and precise parallaxes, although the discrepancy varies on a case-by-case basis. This discrepancy is especially relevant for systems where at least one star has a mass close to $0.45 M_{\odot}$, which is the mass we used to transition between a carbon–oxygen or

⁵See <https://github.com/JamesMunday98/CloseDWDbinaries> (Munday et al. 2024).

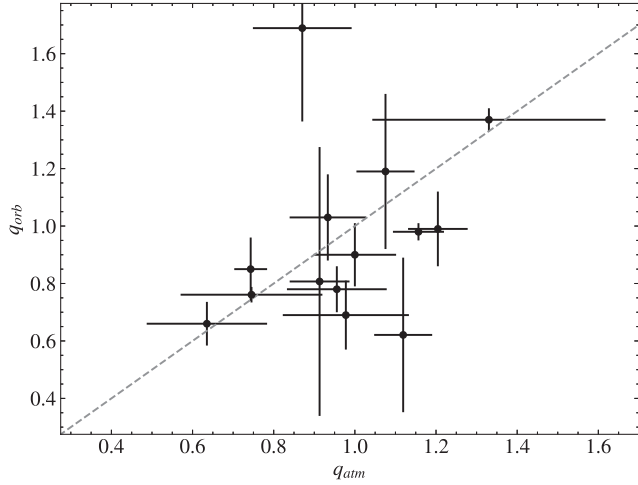


Figure 6. A comparison of the mass ratios deduced from the orbital solution and the fitting of synthetic spectra to obtain atmospherically determined masses. The dashed line represents $q_{\text{orb}} = q_{\text{atm}}$.

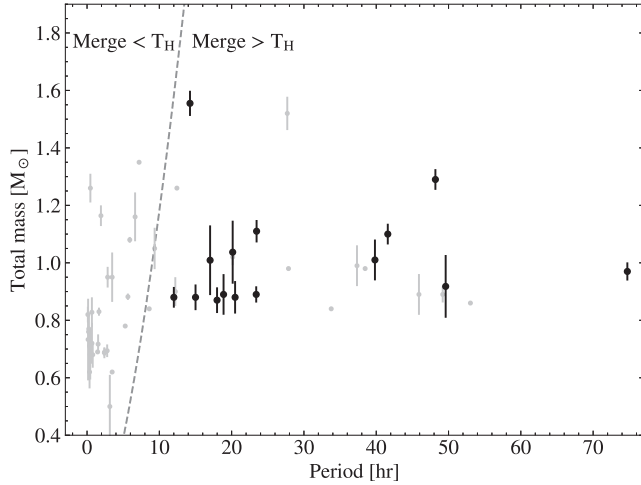


Figure 7. The total mass versus orbital period distribution of the observed sample of DWDs. The points in grey circles are systems in the literature that are eclipsing or double-lined, whereas the black crosses are systems with orbital solutions reported in this work. The dashed grey line is, for two stars of equal mass, the boundary for a binary merging within a Hubble time (T_H). One double-lined DWD (PG1115+166; Bergeron & Liebert 2002) is not plotted for clarity because of its approximately 30-d orbital period (Maxted et al. 2002). The total masses of the targets that fall within the DBL survey are restricted to approximately $0.8\text{--}2.0 M_{\odot}$ because of the Hertzsprung–Russell diagram cuts imposed.

a helium-core mass–radius relationship in the atmospheric parameter fitting.

With our selection of DWDs having similar masses for both stars, the total masses of the DBL systems characterized in this work mostly fall around $1.0 M_{\odot}$, as shown in Fig. 7. In comparison with other double-lined or eclipsing systems in the literature (which, generally speaking, are those with accurate masses for both components), the systems investigated in this paper double the number of compact DWDs with an orbital period above 10 h. This much better reflects the expectations of synthetic populations. All of these newly characterized systems will merge in more than a Hubble time, with one

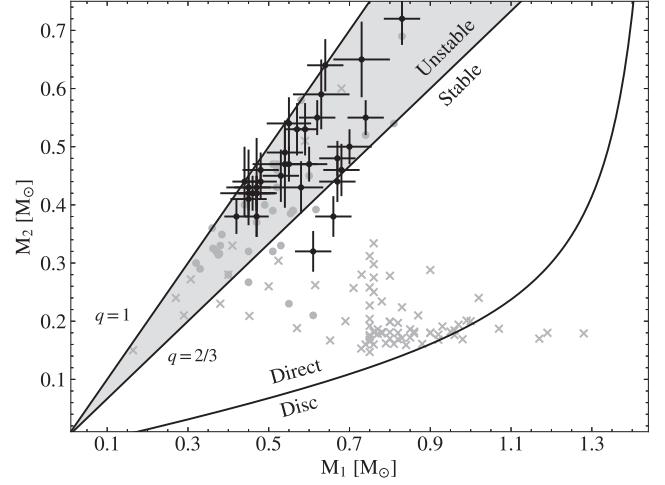


Figure 8. The location of all DBL survey double-lined systems (black) versus other systems in the literature (grey) when comparing a future stable versus unstable mass transfer scenario and whether disc or direct accretion will eventually take place. The literature points denoted by circles are double-lined DWDs and crosses are single-lined DWDs. Direct impact accretion occurs when the trajectory of the accretion stream collides with the surface of the accretor, serving as an angular momentum sink that speeds up the inspiral of a binary, and observationally recognized by strong electromagnetic pulses on the orbital period.

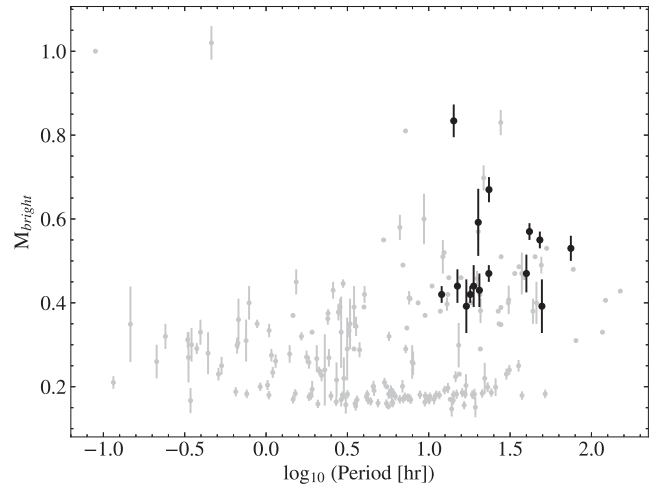


Figure 9. The mass of the brighter star in DWD binaries compared with the orbital period. The systems that are clumping with $M_{\text{bright}} = 0.2 M_{\odot}$ are ELM binaries that are confirmed to be DWDs stemming largely from the ELM survey (Brown et al. 2020; Kosakowski et al. 2023). These primarily form from the mass transfer sequence of a common envelope followed by stable Roche lobe overflow. The brightest absolute magnitude possible for a target found in the DBL survey is similar to a $0.4 M_{\odot}$ DA WD evolutionary sequence for a helium-core mass–radius relationship, making $0.35\text{--}0.4 M_{\odot}$ the minimum mass of the brighter component.

notable exception being WDJ170120.99–191527.57, which has an unclear orbital solution. With a mass ratio close to one, unstable mass transfer will likely cause a merger in the future of these binaries, leading to an R CrB star or a larger mass, single WD. We show how close each system is to the boundary of stable and unstable mass transfer in Fig. 8. WDJ181058.67+311940.94 will also initiate unstable mass transfer, but its total mass significantly

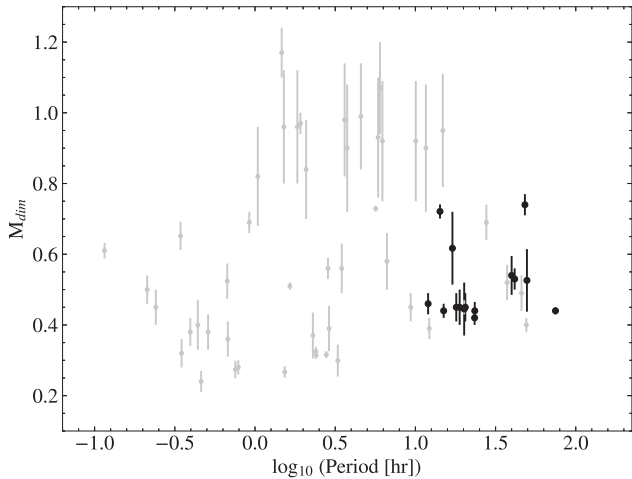


Figure 10. The same as Fig. 9, but for the dimmer star of the binary (M_{dim}). We limit plotting of the literature systems where the fractional error of the mass of the dimmer star is below 20 per cent for the purpose of clarity, which appreciably removes cases around $0.8\text{--}1.0 M_{\odot}$.

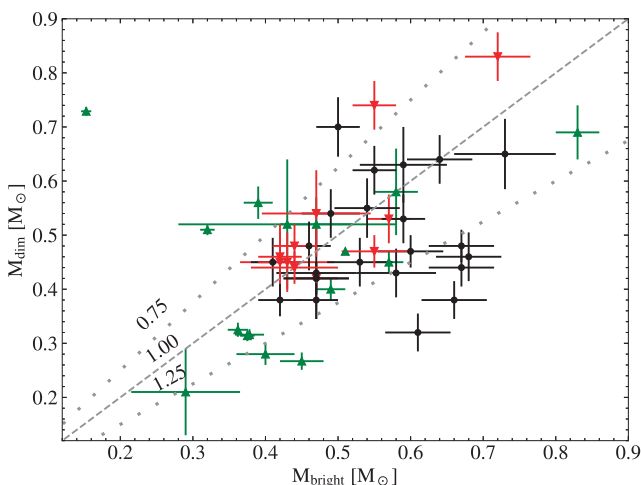


Figure 11. A comparison of the mass of the brighter (more luminous) and dimmer component for well-characterized DWDs. The downward-facing red triangles are systems with complete orbital solutions discussed in Section 4.1. Black points are all other systems presented in the DBL survey I. The upward-facing green triangles are other eclipsing or double-lined systems found in the literature. The dotted lines are ratios of $M_{\text{bright}}/M_{\text{dim}} = 0.75, 1.00,$ and 1.25 .

exceeds the Chandrasekhar mass limit, inevitably giving rise to a Type Ia supernova explosion before the merger event (Munday et al. 2025).

Fig. 9 again shows the orbital periods of the DWD sample but compared with the mass of the brighter star, while Fig. 10 depicts the mass of the dimmer star. A trend of an increasing mass of the brighter star with an increasing orbital period is slightly evident for the presented DBL survey sources (besides the one case of WDJ181058.67+311940.94). This likely appears because mass transfer initiated later for the systems showing longer orbital periods after the common envelope phase, allowing the WD progenitor to grow to higher core masses. The trend here can be a powerful tool in constraining an empirical relationship for the final separation of DWDs exiting the common envelope phase, and with this a

correlation with the core mass of the former giant star, but it is difficult to draw strong conclusions with the sample size.

Additionally, a graphical representation of the masses of the brighter and dimmer stars in the orbitally solved binaries from this paper can be found in Fig. 11. A concentration of systems can be seen following the trend $M_{\text{bright}}/M_{\text{dim}} = 1.25$. Overall, about one-quarter of the 34 double-lined systems give a brighter star that is more massive. This situation can arise from the ‘formation reversal channel’ (Toonen et al. 2012), in which the first mass transfer phase initially forms a helium star, which then cools to become a WD, thus delaying the star’s arrival to the cooling sequence and making it appear younger than the later-formed companion WD. The large fraction of these systems in our survey could be an artefact of the magnitude limit employed in the DBL survey, rather than being reflective of the full DWD population, as the first-formed WD remains brighter for longer in this evolutionary channel.

6 CONCLUSIONS

We have presented a continuation of the DBL survey, supplying orbital solutions for 15 double-lined DWD binaries, and we have narrowed down the viable period aliases for a further six DWDs. These systems cover a wide range of orbital periods for compact DWD binaries, spreading between $P = 5$ and 75 h. We directly analysed the compatibility of the mass ratio derived from the orbital solutions with the mass ratio determined from spectral fitting, finding a good agreement with the values deduced from identification spectra alone. Hence, this emphasizes the potential power of hybrid (combined photometric and spectroscopic) fitting in deducing a mass distribution of double-lined DWDs in wide-scale searches through medium-resolution spectra.

Ultimately, we have taken the first steps in obtaining a mass-period distribution of double-lined DWDs that lie within the selection criteria of the DBL survey, outlined in Munday et al. (2024). This will be a powerful tool to calibrate synthetic population models of DWDs when exploring systems where the mass of the brighter WD exceeds approximately $0.4 M_{\odot}$. In future work, we will aspire to build a larger and more robust sample towards this goal, in terms of both orbital characterization and identification of new double-lined DWDs.

ACKNOWLEDGEMENTS

We thank Yuri Beletsky for support in obtaining spectra from MagE on the Magellan Baade telescope. JM was supported by funding from a Science and Technology Facilities Council (STFC) studentship. IP acknowledges support from a Royal Society University Research Fellowship (URF\R1\231496). This research received funding from the European Research Council under the European Union’s Horizon 2020 research and innovation programme number 101002408 (MOS100PC). DJ acknowledges support from the Agencia Estatal de Investigación del Ministerio de Ciencia, Innovación y Universidades (MCIU/AEI) under grant ‘Nebulosas planetarias como clave para comprender la evolución de estrellas binarias’ and from the European Regional Development Fund (ERDF) with reference PID-2022-136653NA-I00 (DOI:10.13039/501100011033). DJ also acknowledges support from the Agencia Estatal de Investigación del Ministerio de Ciencia, Innovación y Universidades (MCIU/AEI) under grant ‘Revolucionando el conocimiento de la evolución de estrellas poco masivas’ and from the European Union NextGenerationEU/PRTR with reference CNS2023-143910 (DOI:10.13039/501100011033). MK acknowledges support from the National Science Foundation

(NSF) under grant AST-2205736 and the NASA under grants 80NSSC22K0479, 80NSSC24K0380, and 80NSSC24K0436. By NASA through the NASA Hubble Fellowship grant HST-HF2-51527.001-A awarded by the Space Telescope Science Institute, which is operated by the Association of Universities for Research in Astronomy, Inc., for NASA, under contract NAS5-26555. ST acknowledges support from the Netherlands Research Council NWO (VIDI 203.061 grant). For the purpose of open access, the authors have applied a creative commons attribution (CC BY) licence to any author accepted manuscript version arising.

The Isaac Newton Telescope and the William Herschel Telescope are operated on the island of La Palma by the Isaac Newton Group of Telescopes in the Spanish Observatorio del Roque de los Muchachos of the Instituto de Astrofísica de Canarias. Based on observations made with the Nordic Optical Telescope (NOT), owned in collaboration by the University of Turku and Aarhus University, and operated jointly by Aarhus University, the University of Turku and the University of Oslo, representing Denmark, Finland and Norway, the University of Iceland and Stockholm University at the Observatorio del Roque de los Muchachos, La Palma, Spain, of the Instituto de Astrofísica de Canarias. The data presented here were obtained in part with ALFOSC, which is provided by the Instituto de Astrofísica de Andalucía (IAA) under a joint agreement with the University of Copenhagen and NOT. This paper includes data gathered with the 6.5-m Magellan Telescopes located at Las Campanas Observatory, Chile.

Based on observations obtained at the international Gemini Observatory, a programme of NSF's NOIRLab, which is managed by the Association of Universities for Research in Astronomy (AURA) under a cooperative agreement with the NSF on behalf of the Gemini Observatory partnership: the NSF (United States), National Research Council (Canada), Agencia Nacional de Investigación y Desarrollo (Chile), Ministerio de Ciencia, Tecnología e Innovación (Argentina), Ministério da Ciência, Tecnologia, Inovações e Comunicações (Brazil), and Korea Astronomy and Space Science Institute (Republic of Korea).

DATA AVAILABILITY

Measured RVs are given in Appendix B. Raw spectra are obtainable through the respective telescope's public data archive. Reduced spectra will be made available upon request to the lead author.

REFERENCES

- Amaro-Seoane P. et al., 2017, preprint (arXiv:1702.00786)
 Amaro-Seoane P. et al., 2023, *Living Reviews in Relativity*, 26, 2
 Bellm E. C. et al., 2019, *PASP*, 131, 018002
 Bergeron P., Liebert J., 2002, *ApJ*, 566, 1091
 Brown W. R. et al., 2020, *ApJ*, 889, 49
 Calcaferro L. M., Althaus L. G., Córscico A. H., 2018, *A&A*, 614, A49
 Carvalho G. A. et al., 2022, *ApJ*, 940, 90
 Cumming A., 2004, *MNRAS*, 354, 1165
 Drake A. J. et al., 2009, *ApJ*, 696, 870
 Gaia Collaboration et al., 2023, *A&A*, 674, A1
 Ge H., Hjellming M. S., Webbink R. F., Chen X., Han Z., 2010, *ApJ*, 717, 724
 Ge H., Webbink R. F., Chen X., Han Z., 2015, *ApJ*, 812, 40
 Ge H., Webbink R. F., Chen X., Han Z., 2020, *ApJ*, 899, 132
 Heintz T. M., Hermes J. J., Tremblay P. E., Ould Rouis L. B., Reding J. S., Kaiser B. C., van Saders J. L., 2024, *ApJ*, 969, 68
 Hermes J. J. et al., 2014, *ApJ*, 792, 39
 Istrate A. G., Marchant P., Tauris T. M., Langer N., Stancliffe R. J., Grassitelli L., 2016, *A&A*, 595, A35

- Kalogera V., Baym G., 1996, *ApJ*, 470, L61
 Kilic M., Bédard A., Bergeron P., Kosakowski A., 2020, *MNRAS*, 493, 2805
 Kilic M., Bédard A., Bergeron P., 2021, *MNRAS*, 502, 4972
 Kosakowski A., Brown W. R., Kilic M., Kupfer T., Bédard A., Gianninas A., Agüeros M. A., Barrientos M., 2023, *ApJ*, 950, 141
 Li Z., Chen X., Chen H.-L., Han Z., 2019, *ApJ*, 871, 148
 Li Z., Chen X., Ge H., Chen H.-L., Han Z., 2023, *A&A*, 669, A82
 Liebert J., Bergeron P., Holberg J. B., 2005, *ApJS*, 156, 47
 Lipunov V. M., Postnov K. A., Prokhorov M. E., 1987, *A&A*, 176, L1
 Liu Z.-W., Röpke F. K., Han Z., 2023, *Res. Astron. Astrophys.*, 23, 082001
 Lomb N. R., 1976, *Ap&SS*, 39, 447
 Luo J. et al., 2016, *Class. Quantum Gravity*, 33, 035010
 Marsh T. R., 1989, *PASP*, 101, 1032
 Marsh T. R., 2001, *MNRAS*, 324, 547
 Marsh T. R., 2011, *Class. Quantum Gravity*, 28, 094019
 Marsh T., 2019, molly: 1D astronomical spectra analyzer, Astrophysics Source Code Library, record ascl:1907.012 (ascl:1907.012)
 Marshall J. L. et al., 2008, *Proc. SPIE*, 7014, 701454
 Maxted P. F. L., Burleigh M. R., Marsh T. R., Bannister N. P., 2002, *MNRAS*, 334, 833
 McCleery J. et al., 2020, *MNRAS*, 499, 1890
 Munday J. et al., 2024, *MNRAS*, 532, 2534
 Munday J. et al., 2025, *Nat. Astron.*, 9, 872
 Napiwotzki R. et al., 2002, *A&A*, 386, 957
 Nelemans G., Yungelson L. R., Portegies Zwart S. F., Verbunt F., 2001a, *A&A*, 365, 491
 Nelemans G., Yungelson L. R., Portegies Zwart S. F., 2001b, *A&A*, 375, 890
 Nelemans G. et al., 2005, *A&A*, 440, 1087
 Paczynski B., 1976, in Eggleton P., Mitton S., Whelan J. eds, *Proc. IAU Symp. Vol. 73, Structure and Evolution of Close Binary Systems*. Reidel, Dordrecht, p. 75
 Peters P. C., 1964, *Physical Review*, 136, 1224
 Piro A. L., 2019, *ApJ*, 885, L2
 Prochaska J. et al., 2020, *The Journal of Open Source Software*, 5, 2308
 Rebassa-Mansergas A., Toonen S., Korol V., Torres S., 2019, *MNRAS*, 482, 3656
 Ricker G. R. et al., 2015, *J. Astron. Telesc. Instrum. Syst.*, 1, 014003
 Rüter A. J., Seitzzahl I. R., 2025, *A&A Rev.*, 33, 1
 Rüter A. J., Belczynski K., Benacquista M., Larson S. L., Williams G., 2010, *ApJ*, 717, 1006
 Sajadian S., 2025, *AJ*, 169, 164
 Scargle J. D., 1982, *ApJ*, 263, 835
 Scherbak P., Fuller J., 2023, *MNRAS*, 518, 3966
 Tonry J. L. et al., 2018, *PASP*, 130, 064505
 Toonen S., Nelemans G., Portegies Zwart S., 2012, *A&A*, 546, A70
 Toonen S., Hollands M., Gänsicke B. T., Boekholt T., 2017, *A&A*, 602, A16
 Tremblay P. E., Ludwig H. G., Steffen M., Freytag B., 2013, *A&A*, 559, A104
 Tremblay P. E., Gianninas A., Kilic M., Ludwig H. G., Steffen M., Freytag B., Hermes J. J., 2015, *ApJ*, 809, 148
 Webbink R. F., 1984, *ApJ*, 277, 355

SUPPORTING INFORMATION

Supplementary data are available at *MNRAS* online.

suppl_data

Please note: Oxford University Press is not responsible for the content or functionality of any supporting materials supplied by the authors. Any queries (other than missing material) should be directed to the corresponding author for the article.

APPENDIX A: SPECTROSCOPIC FIT TO WDJ170120.99–191527.57

With the new and higher-quality data described in Section 3.2, we present in Fig. A1 the atmospheric fit to this double-lined DWD.

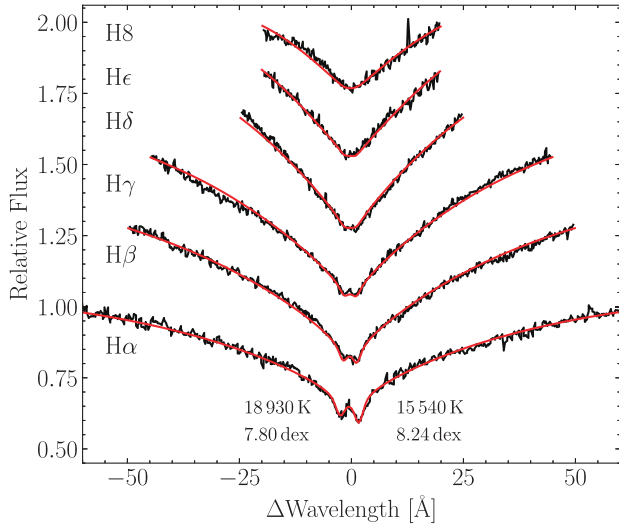


Figure A1. The spectroscopic fit (red) overlaid on a Magellan/MagE spectrum (black) of WDJ170120.99–191527.57 from the Balmer lines H α to H8. The atmospheric parameters for the two stars are labelled; here, the bluishifted star is hotter and less massive.

APPENDIX B: RADIAL VELOCITIES OF FULLY SOLVED DOUBLE-LINED SYSTEMS

Tables B1, B2, B3, B4, B5, B6, B7, B8, B9, B10, B11, B12, B13, and B14 give the observed RVs of every source with a solved orbit or with a confined list of period aliases.

Table B1. RVs for the target WDJ002602.29–103751.86.

HJD 245 0000	ΔRV_1 (km s $^{-1}$)	RV_1 (km s $^{-1}$)	RV_2 (km s $^{-1}$)	ΔRV_2 (km s $^{-1}$)
8363.05908	+85.8	± 4.2	-38.3	± 14.1
8366.06724	+112.8	± 4.2	-55.0	± 23.2
8366.08471	+112.3	± 4.4	-69.9	± 52.1
8726.12643	-4.5	± 11.0	-5.2	± 40.5
8726.14740	+6.3	± 12.9	+75.5	± 53.8
8726.17061	-24.0	± 8.8	+39.7	± 42.2
8726.19158	-41.6	± 12.0	+87.0	± 43.9
8726.21485	-48.9	± 10.8	+70.9	± 30.6
8726.23582	-65.3	± 9.7	+60.6	± 50.5
8729.08342	-5.3	± 9.5	-21.1	± 48.0
8729.10441	-28.0	± 11.7	+41.8	± 33.7
8730.15279	-65.6	± 9.2	+122.8	± 54.7
8730.17377	-83.9	± 10.0	+19.9	± 51.9
8730.19727	-89.3	± 9.5	+18.3	± 45.0
8732.04642	-25.7	± 16.2	+18.8	± 40.4
8750.02581	+14.4	± 10.9	+82.6	± 19.4
8750.04678	+36.5	± 10.3	-67.6	± 36.3
10699.82972	-79.5	± 7.0	+54.8	± 25.6
10699.85443	-59.3	± 7.9	+20.7	± 29.2
10700.83261	-64.9	± 10.3	+9.1	± 42.5
10700.85732	-61.4	± 17.1	+40.2	± 43.2
10701.83575	-53.3	± 8.7	+48.4	± 45.0

Table B2. RVs for the target WDJ005413.14+415613.73.

HJD 245 0000	ΔRV_1 (km s $^{-1}$)	RV_1 (km s $^{-1}$)	RV_2 (km s $^{-1}$)	ΔRV_2 (km s $^{-1}$)
8359.22546	-29.3	± 2.9	+88.0	± 4.9
8361.16421	+148.3	± 3.3	-43.3	± 3.1
8723.09082	+124.1	± 11.9	-18.2	± 16.6
8723.11179	+120.5	± 5.1	-23.4	± 10.5
8723.13841	+87.9	± 6.2	+2.9	± 8.0
8723.15938	+64.9	± 11.4	+8.6	± 13.5
8723.18289	+56.6	± 7.5	+21.0	± 12.3
8723.20386	+37.5	± 5.6	+38.0	± 12.9
8724.23697	-96.5	± 4.0	+159.2	± 6.4
8724.25795	-95.3	± 33.9	+135.6	± 35.6
8725.01340	-51.5	± 4.5	+127.7	± 9.1
8725.03438	-65.8	± 3.9	+125.8	± 7.3
8725.05750	-72.3	± 4.1	+129.9	± 8.2
8725.07848	-90.0	± 4.9	+135.8	± 7.9
8750.95723	+56.5	± 15.6	-34.0	± 24.9
8751.01084	+54.4	± 25.1	+3.9	± 16.3
8751.08709	+126.5	± 23.7	-28.0	± 18.1
8751.10808	+161.5	± 21.9	+4.1	± 26.1
8751.12909	+136.3	± 14.1	-17.4	± 21.9

Table B3. RVs for the target WDJ013812.93+444252.10.

HJD 245 0000	ΔRV_1 (km s $^{-1}$)	RV_1 (km s $^{-1}$)	RV_2 (km s $^{-1}$)	ΔRV_2 (km s $^{-1}$)
8359.20729	-1.6	± 2.2	+39.5	± 7.3
8361.19638	-58.9	± 3.0	+110.3	± 6.0
8361.21038	-53.9	± 3.3	+115.9	± 7.5
8723.23426	-15.9	± 12.0	+84.4	± 10.6
8723.25524	-74.6	± 31.3	+57.8	± 32.3
8724.04965	+50.6	± 7.8	+29.4	± 17.2
8724.07063	+67.5	± 9.0	-12.4	± 11.8
8724.09390	+70.7	± 7.4	-4.1	± 26.9
8724.11487	+62.5	± 8.2	-41.6	± 18.2
8724.14170	+81.9	± 6.3	-51.2	± 24.3
8724.16268	+60.9	± 9.6	-60.2	± 18.2
8724.18599	+82.2	± 11.2	-38.7	± 26.4
8724.20696	+94.1	± 8.9	-55.6	± 17.5
8726.98848	-55.5	± 8.7	+75.4	± 33.2
8727.00947	-57.3	± 11.4	+96.5	± 14.2
8731.15622	+90.3	± 5.5	-76.4	± 13.4

Table B4. RVs for the target WDJ020847.22+251409.97.

HJD 245 0000	ΔRV_1 (km s ⁻¹)	RV_1 (km s ⁻¹)	RV_2 (km s ⁻¹)	ΔRV_2 (km s ⁻¹)
8359.17717	+128.8	±1.6	-30.3	±7.1
8361.18090	+130.1	±1.7	-31.9	±8.1
8362.23391	-27.0	±1.7	+105.8	±6.2
8364.25678	-24.3	±1.7	+109.5	±5.3
8732.06703	+65.9	±6.1	+3.2	±28.7
8732.07759	+70.9	±3.8	+1.0	±23.8
8732.12265	+75.4	±5.2	+13.2	±16.4
8732.13321	+87.0	±5.0	-13.4	±20.0
8732.14619	+84.8	±5.5	-16.3	±21.0
8732.15675	+89.5	±4.5	-2.3	±11.1
8733.13824	+45.9	±16.3	-37.0	±99.9
8733.14880	+10.8	±13.4	+92.9	±85.1
8733.16157	+6.9	±11.4	+71.1	±77.8
8733.17214	+19.1	±12.1	+73.0	±66.7
8734.11706	+70.2	±3.1	+15.2	±11.8
8734.13803	+82.5	±2.6	-7.4	±9.8
8734.15596	+90.2	±3.0	-0.1	±12.0
8734.16652	+92.4	±4.1	-1.8	±11.4
8734.17855	+95.4	±5.0	+7.4	±13.2
8750.15523	+77.4	±2.8	-17.6	±7.7
8750.16578	+76.2	±3.1	-23.8	±17.6
8750.17634	+73.2	±3.9	-31.9	±12.5
8750.18690	+78.7	±3.5	-6.7	±13.8
8751.03389	+43.0	±8.9	+93.8	±47.8
8751.04445	+64.2	±8.8	+30.5	±55.1
8751.05501	+72.3	±9.0	-27.2	±27.0
8751.06557	+44.2	±9.0	+85.1	±44.2
10214.06255	+125.6	±3.7	-45.3	±15.1
10214.06848	+142.2	±5.0	-54.9	±22.9
10214.07441	+130.6	±4.5	-15.2	±13.4
10214.08034	+135.1	±4.2	-1.9	±16.1
10214.18215	+131.1	±4.9	-34.3	±15.1
10214.18924	+134.8	±5.0	-44.2	±12.7
10214.19690	+126.2	±3.7	-37.0	±36.7
10214.20399	+136.7	±4.1	-13.8	±21.2
10233.95335	+88.6	±4.0	-35.1	±14.1
10233.96102	+110.9	±4.2	+1.2	±17.2
10233.96813	+114.4	±3.9	+11.8	±11.1
10233.97523	+99.2	±4.0	-48.0	±13.2
10233.98290	+104.2	±3.6	+0.3	±11.7
10234.01358	+128.1	±3.9	+0.4	±18.3
10234.02069	+114.2	±3.8	-19.2	±8.8
10234.02780	+121.4	±4.5	-7.2	±11.6
10234.03535	+130.3	±4.8	-41.4	±41.7
10234.08485	+130.7	±4.8	-41.7	±15.7
10234.09195	+120.0	±3.8	-64.7	±12.6
10234.09906	+153.5	±4.6	-7.3	±19.8
10234.10662	+131.2	±3.8	-45.5	±17.5
10234.11390	+131.0	±4.4	-18.7	±14.2
10234.16524	+131.2	±4.3	-64.6	±18.0
10234.17235	+137.9	±4.4	-22.4	±14.5
10234.17946	+125.4	±4.1	-38.1	±12.6
10234.18714	+140.1	±5.2	+7.7	±15.9
10234.19424	+116.5	±3.8	-25.4	±10.3

Table B5. RVs for the target WDJ114446.16+364151.13.

HJD 245 0000	ΔRV_1 (km s ⁻¹)	RV_1 (km s ⁻¹)	RV_2 (km s ⁻¹)	ΔRV_2 (km s ⁻¹)
8644.88861	+100.1	±3.5	-66.0	±5.0
8644.90609	+106.5	±3.5	-76.5	±4.3
8645.89599	+0.6	±2.5	-2.1	±4.7
9007.92584	-68.9	±10.2	+125.5	±16.9
9007.93176	-72.7	±11.8	+105.6	±8.5
9008.91465	+8.2	±11.7	-33.2	±23.8
9008.92058	-3.6	±5.8	-13.8	±17.9
9008.92746	-14.8	±15.1	+0.6	±34.8
9008.93338	-7.1	±4.4	-8.9	±14.8
9008.97623	+53.1	±20.4	-57.8	±33.3
9008.98216	+77.3	±21.3	-43.5	±35.4
9010.88005	-0.0	±28.9	+33.1	±30.1
9010.88598	-82.4	±18.7	+80.3	±27.3
9012.96409	+61.0	±20.7	-90.3	±14.9
9012.97117	+56.1	±14.7	-93.2	±34.6
10034.98744	+109.1	±37.4	-106.5	±30.1
10034.99916	+66.1	±32.7	-92.4	±55.6
10035.01088	+110.1	±16.2	-108.6	±45.3
10035.09578	-13.8	±9.9	-18.4	±32.9
10035.10749	+1.3	±6.6	-6.5	±37.0
10035.99829	-86.5	±30.6	+39.8	±34.7
10036.01000	-132.0	±28.0	+135.2	±24.4
10036.02172	-156.1	±13.3	+75.9	±33.5
10036.03412	-85.9	±21.1	+128.6	±34.1
10425.89014	+62.5	±13.1	-64.7	±20.6
10425.91157	+74.1	±15.8	-114.5	±25.8
10425.93311	+85.2	±6.4	-115.3	±14.1
10426.88854	+43.9	±15.5	-47.2	±22.1
10426.91003	+29.7	±11.2	-25.6	±18.5
10426.93149	+3.9	±7.3	+4.9	±11.4
10426.95653	-16.1	±9.1	+15.2	±19.3
10426.97801	-11.8	±13.0	+61.1	±17.0
10426.99960	-42.3	±11.2	+84.7	±12.8
10429.95934	-15.9	±19.7	+15.5	±19.9
10429.98088	-40.1	±22.5	+48.5	±15.5
10430.00272	-40.0	±15.5	+81.4	±14.7
10430.87167	-76.0	±11.9	+137.4	±8.3
10430.89760	-84.6	±8.5	+111.4	±9.5
10430.91913	-74.2	±18.2	+102.6	±14.1
10431.91069	+79.9	±21.2	-111.5	±17.4
10431.93222	+59.4	±20.6	-127.9	±11.0
10431.94791	+141.4	±35.9	-119.8	±13.8
10431.97491	+100.0	±18.3	-151.3	±20.7
10431.99643	+105.8	±10.4	-144.0	±16.1

Table B6. RVs for the target WDJ141625.94+311600.55.

HJD 245 0000	ΔRV_1 (km s ⁻¹)	RV_1 (km s ⁻¹)	RV_2 (km s ⁻¹)	ΔRV_2 (km s ⁻¹)
8590.01924	-41.3	±14.8	+150.1	±10.0
8590.03557	-59.0	±20.8	+113.8	±12.6
8590.96439	+107.8	±9.9	-36.7	±6.7
8590.98072	+112.9	±9.2	-24.2	±8.6
8671.89349	+17.6	±10.6	+44.8	±8.8
10342.17825	+44.4	±13.4	+2.1	±10.4
10342.20083	+100.6	±20.9	+23.4	±13.9
10342.22315	+131.1	±16.0	-1.0	±12.0
10342.26459	+108.9	±9.8	-47.7	±7.0
10429.87151	+37.8	±14.3	+33.7	±7.6
10429.89300	+20.2	±11.9	+20.9	±10.6
10429.91455	+21.1	±22.4	+20.6	±15.3
10429.93606	+38.3	±16.3	+47.6	±10.5
10430.02894	-80.5	±16.6	+93.8	±16.5
10430.05352	-113.0	±23.0	+116.6	±11.6
10430.07766	-95.7	±42.9	+124.8	±14.4
10430.09926	-108.4	±12.3	+55.1	±33.3
10430.12075	-110.6	±12.2	+135.3	±16.1
10430.94581	-55.2	±26.4	+77.0	±21.3
10430.96679	-84.5	±19.9	+97.9	±20.7
10430.98832	-58.0	±21.9	+56.0	±23.8
10432.98031	+14.5	±16.0	+18.2	±8.6
10433.00185	+28.5	±9.3	+28.6	±7.5
10699.23763	-95.4	±11.6	+112.9	±10.3
10700.21245	+94.1	±14.9	+10.3	±12.8
10700.23370	+89.0	±13.8	-6.2	±18.1
10701.22036	+121.7	±7.2	-16.9	±12.8
10701.24160	+114.8	±6.2	-23.9	±9.0
10701.26283	+84.1	±18.2	+13.8	±22.3
10702.15219	-50.1	±7.7	+86.4	±8.0
10702.17342	-54.1	±13.3	+88.1	±6.6
10702.22994	-93.7	±13.2	+113.5	±12.6
10703.12908	-70.0	±5.3	+96.9	±9.9

Table B7. RVs for the target WDJ151109.90+404801.18. Timestamps with asterisks next to the numbers indicate cases where it is unclear if the star 1/2 assignments are correct.

HJD 245 0000	ΔRV_1 (km s ⁻¹)	RV_1 (km s ⁻¹)	RV_2 (km s ⁻¹)	ΔRV_2 (km s ⁻¹)
8645.04282	+80.1	±6.2	-61.0	±5.9
8645.05684	+70.8	±2.8	-64.7	±2.5
*10035.13492	+27.2	±17.6	-121.7	±22.1
*10035.15670	+33.1	±20.1	-81.8	±13.6
*10035.21695	+36.6	±19.2	-46.8	±13.2
*10035.23867	+67.4	±12.4	-29.5	±13.6
*10036.18014	+26.2	±25.8	-44.6	±34.0
10425.95913	-97.0	±11.6	+72.5	±8.5
10425.98056	-68.1	±11.4	+80.2	±7.4
10426.00206	-92.3	±7.0	+77.8	±6.3
10427.02513	-11.4	±16.7	+95.1	±12.2
10427.04667	-7.1	±20.1	+52.1	±62.6
10431.01307	+36.4	±9.9	-55.5	±15.9
10431.03460	-8.7	±12.8	-100.1	±11.5
10431.05606	+10.3	±14.5	-120.0	±17.8
10431.07759	+40.3	±8.9	-99.7	±11.8
10431.19518	+42.7	±9.3	-105.4	±9.0
10431.21661	+44.6	±8.9	-84.0	±6.9
10432.02148	+71.9	±12.7	-45.9	±7.6
10432.04296	+54.3	±10.8	-71.0	±10.0
10432.06449	+62.0	±9.4	-81.5	±14.4
10433.98190	+37.2	±15.7	-77.8	±53.0
10434.00343	+72.9	±9.3	-55.9	±9.6

Table B8. RVs for the target WDJ153615.83+501350.98.

HJD 245 0000	ΔRV_1 (km s ⁻¹)	RV_1 (km s ⁻¹)	RV_2 (km s ⁻¹)	ΔRV_2 (km s ⁻¹)
8645.07514	+77.5	±4.2	+13.4	±7.6
8645.08915	+86.8	±5.8	-26.5	±9.1

Table B9. RVs for the target WDJ160822.19+420543.44.

HJD 245 0000	ΔRV_1 (km s ⁻¹)	RV_1 (km s ⁻¹)	RV_2 (km s ⁻¹)	ΔRV_2 (km s ⁻¹)
8646.08533	-117.4	±2.5	+42.0	±2.4
8646.09240	-110.0	±2.5	+42.9	±3.2
8646.09946	-108.2	±2.4	+34.3	±3.2
8646.11491	-96.0	±1.5	+30.4	±1.7
8646.12745	-82.0	±1.8	+23.5	±2.3
9008.01298	+37.7	±7.2	-68.7	±7.9
9008.02006	+43.8	±6.7	-79.0	±7.9
9008.94875	+88.0	±7.4	-101.9	±7.4
9008.95467	+90.1	±6.1	-106.8	±7.8
9008.96157	+98.2	±7.2	-102.8	±8.8
9008.96749	+103.6	±7.5	-128.3	±10.3
9010.94928	-113.1	±9.7	+36.9	±8.0
9010.95521	-103.3	±11.4	+15.8	±10.7
9012.04518	-118.4	±7.5	+33.5	±9.4
9012.05226	-101.3	±5.1	+36.9	±3.5
9012.12913	-22.9	±6.9	-23.8	±7.9
9012.13621	-20.9	±10.8	-24.7	±11.2
10035.17543	-132.5	±17.9	+39.6	±24.5
10035.18020	-96.6	±15.5	+45.6	±10.6
10035.18497	-108.1	±24.3	+51.6	±26.2
10035.18974	-166.9	±10.9	+49.8	±11.6
10035.25365	-92.1	±27.3	+14.2	±16.9
10036.06601	-101.5	±13.7	+16.9	±15.3
10036.07282	-92.0	±34.1	+30.9	±31.1
10036.07922	-93.1	±12.0	+27.9	±11.8
10036.08561	-53.6	±7.5	+40.8	±5.8
10036.21760	+31.2	±39.1	-12.8	±47.8
10036.22399	+42.9	±15.0	-72.1	±8.2
10036.23038	+61.8	±10.0	-49.7	±16.1
10036.23810	+52.8	±15.2	-98.6	±15.5

Table B10. RVs for the target WDJ163441.85+173634.09.

HJD 245 0000	ΔRV_1 (km s ⁻¹)	RV_1 (km s ⁻¹)	RV_2 (km s ⁻¹)	ΔRV_2 (km s ⁻¹)
8645.10856	+88.7	±2.5	-33.3	±4.4
8645.11563	+88.9	±2.2	-33.5	±3.8
8645.12270	+89.4	±2.1	-31.4	±3.3
9007.98904	-28.8	±7.6	+60.2	±7.9
9007.99612	-35.4	±5.3	+71.5	±7.9
9009.14135	+39.9	±5.9	+13.2	±10.7
9009.14727	+61.8	±4.2	+2.5	±6.9
9010.96912	+73.6	±10.7	-28.8	±18.1
9010.97505	+68.2	±8.6	-44.9	±15.1
9010.98196	+93.8	±8.2	-26.1	±10.6
9010.98788	+62.9	±13.9	-20.4	±16.6
9012.01278	-54.3	±4.8	+69.9	±6.8
9012.01986	-53.3	±5.7	+71.8	±8.8
9012.02791	-51.6	±3.9	+78.0	±5.3
9012.03499	-44.8	±4.9	+74.2	±7.4

Table B11. RVs for the target WDJ182606.04+482911.30.

HJD 245 0000	ΔRV_1 (km s ⁻¹)	RV_1 (km s ⁻¹)	RV_2 (km s ⁻¹)	ΔRV_2 (km s ⁻¹)
8359.92351	+6.2	±6.9	-95.7	±8.8
8367.02429	+36.8	±5.5	-120.6	±13.7
8725.89196	-70.7	±15.7	+87.3	±30.3
8725.91296	-61.2	±22.0	+83.5	±25.7
8725.93608	-101.4	±17.2	+83.7	±30.4
8725.95705	-95.8	±10.5	+72.8	±22.8
8728.98501	-16.4	±9.2	-6.4	±28.7
8729.00601	-12.3	±16.9	-65.9	±42.6
8729.02936	-56.8	±30.1	+31.1	±20.2
8729.05033	-40.1	±22.4	+45.0	±20.4
8733.90809	-5.0	±7.1	-12.0	±37.4
8733.92906	-36.7	±14.0	-67.9	±31.2
10431.09891	+31.1	±14.5	-100.3	±21.3
10431.12044	+20.7	±30.6	-71.5	±39.4
10431.14193	+11.6	±22.3	-100.7	±25.2
10431.16346	+37.2	±12.1	-97.0	±16.3
10432.12048	-15.9	±21.7	-40.0	±18.7
10432.16354	-11.7	±17.1	-73.5	±29.5
10432.18534	+2.9	±17.6	-46.5	±27.4
10433.02499	-32.4	±13.7	+29.4	±37.3
10433.04651	-39.9	±16.8	-5.0	±25.6
10434.02792	+25.5	±20.1	-75.8	±56.3
10434.04937	+68.8	±11.9	-108.7	±14.9
10434.19949	+36.4	±31.7	-123.1	±14.8

Table B12. RVs for the target WDJ183442.33-170028.00.

HJD 245 0000	ΔRV_1 (km s ⁻¹)	RV_1 (km s ⁻¹)	RV_2 (km s ⁻¹)	ΔRV_2 (km s ⁻¹)
8364.89558	-177.2	±3.3	+119.4	±11.2
8366.91659	-133.7	±4.2	+92.7	±12.2
8366.93753	-103.6	±3.6	+67.5	±17.5
8671.00733	-169.2	±4.6	+118.7	±14.4
8671.02375	-154.4	±3.1	+117.0	±13.0
8672.05606	-86.1	±5.6	+103.6	±6.9
9010.05790	-57.4	±17.2	+117.6	±43.9
9010.08582	-24.4	±41.2	+87.7	±54.8
9012.18969	-114.3	±13.0	+149.1	±23.8
9014.07330	-81.0	±11.9	+113.3	±13.3
9014.10122	-130.6	±7.4	+107.7	±16.7
9014.13012	-170.6	±10.2	+168.1	±23.9
9014.15804	-137.8	±15.3	+131.5	±14.4
10432.21371	-45.6	±35.4	+96.6	±69.6
10434.16487	+52.6	±17.5	-34.8	±42.0
10475.10559	+159.9	±25.2	-129.7	±42.9
10475.12747	+123.9	±26.8	-91.0	±58.0

Table B13. RVs for the target WDJ212935.23+001332.26.

HJD245 0000	ΔRV_1 (km s ⁻¹)	RV_1 (km s ⁻¹)	RV_2 (km s ⁻¹)	ΔRV_2 (km s ⁻¹)
8359.07483	+82.0	±4.4	-21.2	±4.8
8367.07114	+134.5	±4.5	-54.4	±6.3
8723.90031	-23.1	±16.0	+63.7	±18.3
8723.92587	+3.1	±24.3	+52.2	±57.1
8723.94684	+29.7	±11.7	+31.4	±16.5
8725.10960	-67.2	±10.0	+110.6	±14.0
8725.13057	-49.6	±7.4	+96.6	±11.7
8725.98813	+139.5	±6.7	-45.9	±12.2
8726.00910	+140.3	±7.0	-65.5	±15.0
8726.03216	+119.0	±7.3	-46.8	±9.0
8726.05313	+119.5	±8.6	-46.0	±22.6
8726.07613	+95.9	±6.9	-33.7	±8.7
8726.09711	+73.4	±7.5	-6.8	±14.6
8730.11932	-37.5	±8.7	+134.8	±18.3

Table B14. RVs for the target WDJ231404.30+552814.11.

HJD 245 0000	ΔRV_1 (km s ⁻¹)	RV_1 (km s ⁻¹)	RV_2 (km s ⁻¹)	ΔRV_2 (km s ⁻¹)
8360.06566	-58.3	±7.6	+42.5	±4.9
8362.16173	+73.8	±5.9	-53.5	±4.8
8362.17920	+59.3	±5.6	-50.4	±4.4
8725.15411	-37.8	±13.8	+28.2	±10.7
8725.17508	-27.5	±15.5	+22.3	±12.6
8725.19819	-5.0	±21.8	+19.5	±16.6
8725.21916	-2.2	±16.8	+4.0	±12.8
8725.24444	+25.9	±13.7	+29.5	±11.7
8727.06440	-34.1	±25.0	+36.5	±17.1
8727.10831	-5.3	±31.2	+10.5	±28.8
8727.12928	-3.5	±33.8	-9.4	±27.7
8727.15169	-47.0	±7.7	+32.0	±10.1
8727.88956	-60.6	±19.5	+82.3	±12.5
8727.91055	-38.1	±10.0	+65.2	±8.5
8727.93548	-44.7	±8.9	+78.9	±10.7
8727.95646	-35.4	±5.8	+96.1	±8.2
8733.11161	+33.7	±15.1	-29.6	±8.8
9794.51103	+72.6	±15.7	-48.5	±13.5
9794.62542	+76.2	±12.2	-62.4	±10.6
9795.38290	-38.5	±14.4	+47.0	±11.1
9795.46051	-70.8	±18.1	+53.6	±12.1
9797.49635	+58.7	±13.0	-72.2	±12.2
9797.59125	+57.2	±14.0	-60.9	±10.0
9799.46266	-18.8	±28.0	-5.9	±31.2
9799.61133	-15.1	±20.5	-17.5	±15.5
9800.56944	+40.8	±15.4	-76.3	±12.6
10817.15999	-94.3	±12.7	+62.0	±10.4
10817.21082	-80.3	±12.0	+58.4	±7.2
10820.14396	-64.5	±7.9	+72.9	±5.4
10820.20666	-68.2	±7.6	+80.1	±5.2
10826.21066	-61.5	±6.6	+68.3	±4.3

APPENDIX C: RADIAL VELOCITIES OF DOUBLE-LINED SYSTEMS WITH PERIOD ALIASES

Tables C1, C2 C3, and C4 are the observed RVs of every source that have multiple viable period aliases.

Table C1. RVs for the target WDJ000319.54+022623.28.

HJD 245 0000	ΔRV_1 (km s ⁻¹)	RV_1 (km s ⁻¹)	RV_2 (km s ⁻¹)	ΔRV_2 (km s ⁻¹)
8671.21502	+56.0	±5.9	+19.8	±16.1
8672.21313	+99.4	±5.0	-51.9	±12.1
8672.22725	+98.3	±4.8	-79.8	±12.2
8727.18346	-10.7	±10.9	+146.0	±24.9
8727.20443	-18.9	±6.8	+113.9	±16.7
8727.22709	-3.5	±5.0	+172.2	±19.4
8727.24806	-9.2	±16.4	+144.6	±29.4
8727.98587	+94.4	±12.7	-12.4	±36.3
8728.00687	+119.7	±12.7	-66.4	±35.0
8728.02931	+131.7	±22.8	-45.2	±45.3
8728.05028	+116.1	±13.5	-47.5	±30.2
8728.07276	+110.4	±14.1	-116.2	±31.2
8728.09373	+104.6	±10.1	-120.0	±13.0
8729.13332	+38.8	±13.8	-14.5	±35.0
8729.15429	+63.0	±8.3	-22.9	±32.9
8729.17799	+67.1	±20.6	-44.8	±33.5
8731.18880	+100.5	±6.9	+20.0	±48.1

Table C2. RVs for the target WDJ080856.79+461300.08.

HJD 245 0000	ΔRV_1 (km s ⁻¹)	RV_1 (km s ⁻¹)	RV_2 (km s ⁻¹)	ΔRV_2 (km s ⁻¹)
8527.96071	+97.8	±22.9	-24.3	±35.9
8534.12860	-16.9	±8.1	+111.7	±11.5
8534.15398	-16.9	±8.7	+88.1	±15.9
10432.86430	+63.0	±13.1	-71.4	±33.5
10432.88574	+76.5	±15.7	-34.8	±54.0
10432.90727	+89.9	±18.3	-10.3	±27.2
10432.92871	+112.1	±13.7	-0.2	±28.6
10432.95016	+103.8	±14.3	-15.9	±19.6
10433.86435	+79.1	±16.6	-25.3	±46.1
10433.88588	+120.9	±12.3	-75.4	±20.9
10433.90923	+127.9	±12.4	-38.4	±26.1
10433.93076	+116.6	±22.9	-54.4	±45.8
10433.95221	+113.4	±18.6	-51.2	±36.4
10461.90284	-29.2	±22.1	+139.2	±30.2
10461.92407	-10.9	±7.8	+133.1	±14.8
10752.97090	+89.5	±12.8	-13.2	±17.4
10753.03265	+66.3	±15.6	-17.3	±25.2

Table C3. RVs for the target WDJ170120.99-191527.57.

HJD 245 0000	ΔRV_1 (km s ⁻¹)	RV_1 (km s ⁻¹)	RV_2 (km s ⁻¹)	ΔRV_2 (km s ⁻¹)
8589.23520	-140.0	±12.4	+102.3	±11.4
8591.15233	+58.1	±6.9	-83.8	±4.6
8591.16866	+116.4	±9.2	-137.4	±5.6
10430.14734	-160.3	±22.4	+98.1	±14.4
10430.16926	-139.4	±18.4	+80.5	±10.7
10430.19189	-150.8	±19.4	+48.9	±18.7
10433.07839	-117.1	±16.2	+80.8	±16.3
10433.10133	-54.8	±15.5	+20.3	±14.2
10433.12283	+44.5	±17.0	-60.3	±14.1
10433.14441	+91.5	±21.1	-129.7	±34.9
10433.16594	+120.0	±10.3	-140.9	±11.6
10434.08238	-148.6	±12.8	+78.1	±11.8
10434.09934	-121.5	±22.7	+93.1	±13.9
10434.11718	-98.7	±41.4	+76.3	±11.3
10434.13872	-31.2	±36.8	-7.4	±25.4
10460.06880	-153.4	±9.9	+112.9	±8.2
10460.07816	-153.5	±14.1	+118.0	±10.0
10460.08723	-113.1	±11.5	+85.7	±8.3
10460.09652	-112.3	±16.1	+59.0	±12.3
10460.10560	-82.8	±13.5	+57.2	±13.0
10460.11494	-55.9	±11.8	+6.9	±13.9
10460.12403	-19.3	±19.2	-16.4	±13.4
10460.13729	+41.9	±15.9	-47.0	±27.3
10460.14663	+80.3	±14.8	-95.6	±12.7
10460.15571	+103.4	±11.6	-112.4	±9.2
10463.05503	+120.4	±17.0	-135.2	±11.8
10463.06403	+99.8	±18.1	-132.9	±13.5
10463.18043	-142.4	±14.6	+103.4	±12.3
10502.10991	-101.8	±3.8	+57.0	±4.3
10502.12407	-120.8	±4.1	+72.7	±3.7

Table C4. RVs for the target WDJ180115.37+721848.76.

HJD 245 0000	ΔRV_1 (km s ⁻¹)	RV_1 (km s ⁻¹)	RV_2 (km s ⁻¹)	ΔRV_2 (km s ⁻¹)
8359.88252	-94.0	±3.9	+106.5	±17.6
8363.86443	+53.6	±3.7	-71.8	±8.9
8363.88191	+61.9	±3.3	-79.0	±7.5
9007.95255	-0.0	±7.8	+1.1	±36.2
9007.96657	-11.3	±13.9	+75.9	±25.7
9009.95799	+109.3	±23.7	-124.7	±55.8
9009.97549	+116.7	±18.8	-127.4	±46.0
9012.92967	-67.7	±12.4	+46.9	±50.8
9012.94647	-77.0	±12.9	+46.8	±31.7
10700.26108	-91.9	±7.8	+100.6	±19.0
10700.28582	-90.6	±5.7	+139.5	±11.8
10701.28668	-45.8	±10.0	+64.8	±42.6
10702.27395	+65.3	±6.8	-92.5	±45.3
10702.29171	+57.9	±10.0	-130.2	±43.7
10703.26520	+108.7	±4.2	-101.5	±19.8
10703.28644	+112.0	±5.0	-104.9	±18.0

Table D1. RVs for all single-lined sources. The first and last five rows of the table are presented and the full table is supplied in the online supplementary material.

Target	HJD 245 0000	RV (km s ⁻¹)	Δ RV (km s ⁻¹)
WDJ001321.07+282019.83	8359.58773	30.14	± 8.56
WDJ001321.07+282019.83	8359.59483	28.52	± 6.55
WDJ001321.07+282019.83	8359.60215	32.48	± 9.24
WDJ001321.07+282019.83	8359.60924	32.81	± 7.38
WDJ001321.07+282019.83	8359.61633	33.83	± 6.43
⋮	⋮	⋮	⋮
⋮	⋮	⋮	⋮
WDJ232557.82+255222.39	8365.61147	10.53	± 7.46
WDJ233041.67+110206.43	8364.60806	47.07	± 3.74
WDJ235313.18+205117.58	8360.66009	28.75	± 3.28
WDJ235313.18+205117.58	8362.55461	26.30	± 4.79
WDJ235313.18+205117.58	8362.57556	30.99	± 2.56

APPENDIX D: RADIAL VELOCITIES OF SINGLE-LINED SOURCES

Table D1 gives the RVs extracted for all single-lined sources observed in the DBL survey where hydrogen Balmer absorption lines are apparent.

This paper has been typeset from a $\text{\TeX}/\text{\LaTeX}$ file prepared by the author.